Least-squares diffraction imaging using shaping regularization by anisotropic smoothing[a]

---

[a] Published in Geophysics, v. 85, S313-S325, (2020)

Dmitrii Merzlikin, Sergey Fomel†, and Xinming Wu‡*

ABSTRACT

We use least-squares migration to emphasize edge diffractions. The inverted forward modeling operator is the chain of three operators: Kirchhoff modeling, azimuthal plane-wave destruction and path-summation integral filter. Azimuthal plane-wave destruction removes reflected energy without damaging edge diffraction signatures. Path-summation integral guides the inversion towards probable diffraction locations. We combine sparsity constraints and anisotropic smoothing in the form of shaping regularization to highlight edge diffractions. Anisotropic smoothing enforces continuity along edges. Sparsity constraints emphasize diffractions perpendicular to edges and have a denoising effect. Synthetic and field data examples illustrate the effectiveness of the proposed approach in denoising and highlighting edge diffractions, such as channel edges and faults.

INTRODUCTION

Diffraction imaging is able to highlight subsurface discontinuities associated with channel edges, fracture swarms and faults. Since diffractions are usually weaker than reflections (Klem-Musatov, 1994) and have lower signal-to-noise ratio, robust diffraction extraction is of utmost importance for the imaging of subtle discontinuities. A number of diffraction imaging methods have been developed and can be classified based on the separation technique being employed. Methods based on optimal stacking of diffracted energy and suppression of reflections are described by Kanasewich and Phadke (1988), Landa and Keydar (1998), Berkovitch et al. (2009), Dell and Gajewski (2011), Tsingas et al. (2011) and Rad et al. (2014). Wavefield separation methods aim to decompose conventional full-wavefield seismic records into different components representing reflections and diffractions (Papziner and Nick, 1998; Taner et al., 2006; Fomel et al., 2007; Schwarz and Gajewski, 2017; Schwarz, 2019; Dell et al., 2019b). Decomposition can be carried out in the common-image gather domain (Reshef and Landa, 2009; Klokov and Fomel, 2012; Silvestrov et al., 2015). Other authors (Kozlov et al., 2004; Moser and Howard, 2008; Koren and Ravve, 2011; Klokov and Fomel, 2013; Popovici et al., 2015) modify migration kernel to eliminate specular energy coming from the first Fresnel zone and image diffractions only. For the methods involving migration, diffraction extraction quality becomes dependent on the velocity model accuracy. Numerous case studies show that diffraction images carry valuable additional information for seismic interpretation (Schoepp et al., 2015; Burnett et al., 2015; Sturzu et al., 2015; Tyiasning et al., 2016; Klokov et al., 2017a,b; Merzlikin et al., 2017b; de Ribet et al., 2017; Pelissier et al., 2017; Koltanovsky et al., 2017; Zelewski et al., 2017; Foss et al., 2018; Glöckner et al., 2019; Moser et al., 2020; Montazeri et al., 2020).

Consideration of diffraction phenomena in 3D (Keller, 1962; Klem-Musatov et al., 2008; Hoeber et al., 2010) requires taking into account edge diffractions. Due to lateral symmetry they kinematically behave as reflections when observed along the edge and as diffractions when observed perpendicular to the edge (Moser, 2011). Thus, edge diffraction signature is neither a "pure" reflection nor a "pure" diffraction but rather a combination of both and therefore requires a special processing procedure to be emphasized. Serfaty et al. (2017) separate reflections, tip and edge diffractions and noise using principal component analysis and deep learning. Klokov et al. (2011) and Bona and Pevzner (2015) investigate 3D signatures of different types of diffractors. Alonaizi et al. (2013) and Merzlikin et al. (2017a) propose workflows to properly process energy diffracted on the edge. Keydar and Landa (2019) propose a method for edge diffraction imaging based on time-reversal principle and the stacking operator directly targeting edge diffractions. Dell et al. (2019a) extract edge diffraction responses from full wavefield data by analyzing amplitude distribution along different azimuths on a 3D prestack time Kirchhoff migration stacking surface. Znak et al. (2019) develop a common-reflection-surface-based framework for distinguishing between point and edge diffractions and separating them from reflections.

Separation of reflections and diffractions can be done as a part of least-squares migration (Nemeth et al., 1999; Ronen and Liner, 2000). Harlan et al. (1984) pioneer in separating diffractions from noise by comparing observed data and data modeled from a migration image in a least-squares sense. Merzlikin and Fomel (2016) perform least-squares migration chained with plane-wave destruction and path-summation integral filtering and enforce sparsity in a diffraction model. Merzlikin et al. (2019) extend the approach and simultaneously decompose the input wavefield into reflections, diffractions and noise. Decker et al. (2017) denoise diffractions by applying semblance-based weights estimated in dip-angle gather (DAG) domain. Yu et al. (2016) utilize common-offset Kirchhoff least-squares migration with a sparse model regularization to emphasize diffractions. Yu et al. (2017a) extract diffractions based on plane wave destruction and dictionary learning for sparse representation. Yu et al. (2017b) use two separate modeling operators for diffractions and reflections and impose a sparsity constraint on diffractions. Sparse inversion is an efficient tool to perform extraction and denoising of diffractions since scatterers have spiky and intermittent distribution. However, a simple sparsity constraint does not account for the signature of the energy scattered on the edge, which is kinematically similar to a reflection when observed along the edge, and thus can distort it.

We combine sparsity constraints and structure-oriented smoothing in the form of shaping regularization (Fomel, 2007) to highlight edge diffractions and account for their signature. Structure-oriented smoothing performs smoothing along the edges emphasizing their continuity (Hale, 2009). Sparsity constraints imposed by thresholding in the model space force the model to describe the data with the fewest parameters and therefore denoise and emphasize edge diffraction signatures observed perpendicular to the edge. Thus, we properly account for edge diffraction kinematic behavior for both parallel and perpendicular to the edge directions.

For forward modeling we use a chain of operators introduced by Merzlikin and Fomel (2016). We extend this workflow to three-dimensions and modify reflection destruction operator to account for an edge diffraction signature by suppressing reflected energy perpendicular to edges. Edge orientations are determined through a plane-wave destruction based structure tensor (Merzlikin et al., 2017a). We start with a method introduction, then validate its performance on a synthetic, on a noisy marine field dataset and on a land field dataset by separating edge diffractions from reflections and noise.

METHOD

Objective function

To solve for a seismic diffraction image $\mathbf{m}_d$, we extend the approach developed by Merzlikin and Fomel (2016) to three dimensions:

$$J(\mathbf{m}_d) = \|\mathbf{d}_{PI} - \mathbf{PDLm}_d\|_2^2, \tag{1}$$

where $J(\mathbf{m}_d)$ is the objective function, $\mathbf{d}_{PI} = \mathbf{PDd}$ and $\mathbf{d}$ is “observed” data. Here, forward modeling corresponds to the chain of operators: three-dimensional path-summation integral filter $\mathbf{P}$ (Merzlikin and Fomel, 2015, 2017), azimuthal plane wave destruction (AzPWD) filter $\mathbf{D}$ (Merzlikin et al., 2016, 2017b) and three-dimensional Kirchhoff modeling $\mathbf{L}$. The path-summation integral filter $\mathbf{P}$ can be treated as the probability of a diffraction at a certain location. Azimuthal plane wave destruction filter $\mathbf{D}$ removes reflected energy perpendicular to the edges. Therefore, AzPWD emphasizes edge diffraction signature, which when measured in the direction perpendicular to the edge exhibits a hyperbolic moveout and kinematically behaves as a reflection when observed along the edge. AzPWD application is the key distinction from the 2D version of the workflow (Merzlikin and Fomel, 2016), in which plane-wave destruction filter (PWD) (Fomel, 2002) is applied along the time-distance plane (Fomel et al., 2007; Merzlikin et al., 2018). After weighting the data $\mathbf{d}_{PI} = \mathbf{PDd}$ by path-summation integral $\mathbf{P}$ and AzPWD filter $\mathbf{D}$, model fitting is constrained to most probable diffraction locations.

Determination of edge diffraction orientation

For AzPWD workflow Merzlikin et al. (2016, 2017b) show that a volume with plane-wave destruction filter applied in arbitrary direction x' corresponding to the azimuth θ can be generated as a linear combination of PWDs applied in inline ($\mathbf{D}_x$) and crossline ($\mathbf{D}_y$) directions: $\mathbf{D}_{x'} = \mathbf{D}_x \cos\theta + \mathbf{D}_y \sin\theta$. Due to migration procedure linearity the same relationship holds for the images of the corresponding PWD volumes. Azimuth θ should be perpendicular to the edge at each location to remove reflections but preserve edge diffraction signatures, which are kinematically similar to reflections when observed along the edge.

This azimuth can be determined from the structure tensor (Van Vliet and Verbeek, 1995; Weickert, 1997; Fehmers and Höcker, 2003; Hale, 2009; Wu, 2017; Wu and Janson, 2017), which is defined as an outer product of migrated plane-wave destruction filter volumes in inline and crossline directions (Merzlikin et al., 2016, 2017b):

$$\mathbf{S} = \begin{bmatrix} \langle p_x p_x \rangle & \langle p_x p_y \rangle \\ \langle p_x p_y \rangle & \langle p_y p_y \rangle \end{bmatrix}, \tag{2}$$

where $\langle\rangle$ denotes smoothing of structure-tensor components, which is done in the edge-preserving fashion (Liu et al., 2010). Smoothing stabilizes structure-tensor orientation determination in the presence of noise (Weickert, 1997; Fehmers and Höcker, 2003), while edge-preservation keeps information related to geologic discontinuities, which otherwise would be lost due to smearing. Here, p_x and p_y are the samples of inline and crossline migrated PWD volumes ($\mathbf{P}_x$ and $\mathbf{P}_y$) at each location. PWD filter can be treated as a derivative along the dominant local slope (Fomel, 2002; Fomel et al., 2007). Thus, a 2D PWD-based structure tensor (equation 2) effectively represents 3D structures without the need for the third dimension because the orientations are determined along the horizons.

Edge orientation can be determined by an eigendecomposition of a structure tensor (Fehmers and Höcker, 2003; Hale, 2009): $\mathbf{S} = \lambda_u \mathbf{u}\mathbf{u}^T + \lambda_v \mathbf{v}\mathbf{v}^T$. If a linear feature (edge) is encountered eigenvector $\mathbf{u}$ corresponding to a larger eigenvalue λ_u points in the direction perpendicular to the edge. Eigenvector $\mathbf{v}$ of a smaller eigenvalue λ_v points along the edge. Thus, azimuth θ of a direction x' perpendicular to the edge can be computed from either $\mathbf{u}$ or $\mathbf{v}$. If no linear features are observed, there is no preferred PWD direction.

The PWD-based tensor (equation 2) describes 3D structures. Its components (p_x and p_y) are computed along the “structural frame” defined by the reflecting horizons. Thus, vectors $\mathbf{u}$ and $\mathbf{v}$ “span” the surfaces, which at each point are determined by dominant local slopes. Eigenvectors of a PWD-based structure tensor (equation 2) are parallel to a reflection surface at each point.

Regularization

We use shaping regularization to constrain the model (Fomel, 2007). We penalize edge diffractions by two shaping operators: thresholding and smoothing by anisotropic diffusion. Iterative application of the first operator forces the model to describe the data with the fewest parameters possible (Daubechies et al., 2004) and therefore denoises and emphasizes edge diffraction signatures in the direction perpendicular to the edge. The second operator emphasizes the signatures of edge diffractions along the edge by enforcing their continuity.

Smoothing based on anisotropic diffusion enhances flow-like structures and completes interrupted lines (Weickert, 1998). The input is an unfiltered image, smoothness of which is increasing while diffusion is proceeding in time (Fehmers and Höcker, 2003). In a discrete form anisotropic diffusion can be formulated as follows:

$$\frac{\mathbf{U}_k - \mathbf{U}_{k-1}}{\Delta t} = -\,\mathbf{D}_{im}^T\,\mathbf{V}\;\mathbf{V}^T\,\mathbf{D}_{im}\,\mathbf{U}_k\;, \tag{3}$$

where $\mathbf{U}_k$ is an image at a diffusion time step k with Δt sampling interval, $\mathbf{D}_{im}$ is a matrix operator combining PWDs in inline and crossline directions in the image domain and $\mathbf{V}$ is a matrix of eigenvectors $\mathbf{v}$, which are parallel to linear features' orientations along the dominant local slopes. Classic anisotropic diffusion partial differential equation (Weickert, 1998) requires three-dimensional structure tensor and gradient. In equation 3, we utilize PWD-based structure tensor instead of its three-dimensional counterpart based on derivatives along the coordinate axes and a combination of PWDs in inline and crossline directions in the image domain instead of a three-dimensional gradient. After terms rearrangement, equation 3 takes the form of a linear least-squares solution with forward modeling operator corresponding to the identity matrix:

$$\mathbf{U}_k = \left(\mathbf{I} + \epsilon^2\,\mathbf{D}_{im}^T\,\mathbf{V}\;\mathbf{V}^T\,\mathbf{D}_{im}\right)^{-1}\,\mathbf{U}_{k-1}\,, \tag{4}$$

where ϵ corresponds to the time step Δt. At diffusion time step k we update the previous image $\mathbf{U}_{k-1}$ with N conjugate gradients iterations until the desired smoothness is achieved in the output image $\mathbf{U}_k$. Total number of diffusion time steps K, number of conjugate gradients iterations N and parameter ϵ control the smoothness of the final result.

Figure 1 shows anisotropic smoothing operator action on a zigzag pattern contaminated with Gaussian noise. Isotropic smoothing operator (see, e.g., Weickert (1998) for details) action is equal for all the directions and thus results in sharpness loss incurred by smoothing across the edges (Figure 1c). Figure 1d shows that anisotropic smoothing operator (equation 4) preserves edges by smoothing along them and thus results in both S/N ratio enhancement and sharpness of the image.

Flow-like coherent noise patterns in Figure 1d are induced by using "true" azimuths of edges across the whole image including both signal and noise regions. The result of combining both regularization operators - thresholding and anisotropic smoothing - is shown in Figure 1f: noise and flow-like artifacts are suppressed in regions with no signal. Thus, the combination of thresholding and anisotropic smoothing is required for proper edge diffraction regularization.

In the following examples, edge orientation estimation is done for each location individually based on a structure tensor.

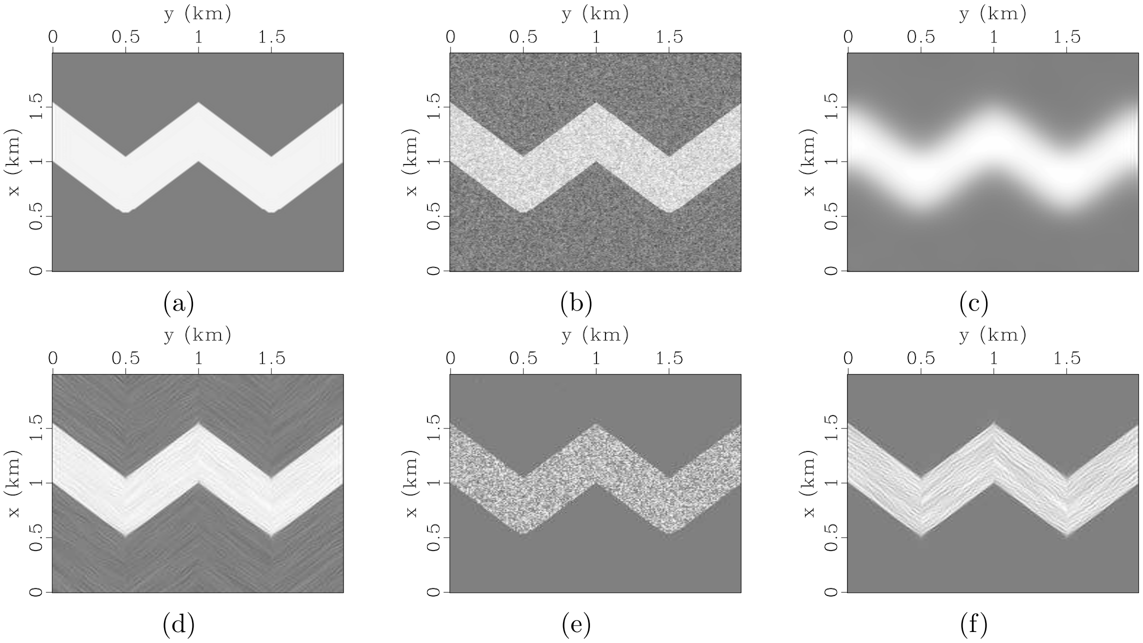

(a) (b) (c) (d) (e) (f)

Figure 1: Zigzag pattern: (a) with no noise; (b) with Gaussian noise added; (c) corresponds to (b) processed by isotropic smoothing operator (notice smoothing across the edges); (d) corresponds to (b) processed by anisotropic smoothing operator (edges are highlighted and preserved). Flow-like coherent noise patterns in (d) are induced by using "true" azimuths of edges across the whole image including both signal and noise regions. Thresholding operator action on (b) is shown in (e). The result of combining both regularization operators - anisotropic smoothing and thresholding - is shown in (f). Noise including flow-like artifacts is attenuated.

Optimization

For inversion we adopt a conjugate gradients scheme (Fomel et al., 2007):

$$\mathbf{m}_d^i \;\leftarrow\; \mathbf{H}_{\epsilon,N,K}\mathbf{T}_\lambda\big[\mathbf{m}_d^j \;+\; \alpha_j\mathbf{s}_j\big],\; \mathbf{s}_j = -\nabla J(\mathbf{m}_d^j) \;+\; \beta_j\mathbf{s}_{j-1} \tag{5}$$

where $\mathbf{H}_{\epsilon,N,K}$ and $\mathbf{T}_\lambda$ are anisotropic-smoothing and thresholding operators, $-\nabla J(\mathbf{m}_d^j)$ is the gradient at iteration j, $\mathbf{s}_j$ is a conjugate direction, α_j is an update step length , and β_j is designed to guarantee that $\mathbf{s}_j$ and $\mathbf{s}_{j-1}$ are conjugate. After several internal iterations j of the conjugate gradient algorithm we generate $\mathbf{m}_d^j$, to which we apply thresholding to drop samples corresponding to noise with values lower than the threshold λ, and which we then smooth along edges by applying anisotropic smoothing operator $\mathbf{H}_{\epsilon,N,K}$. Outer model shaping iterations are denoted by i.

Inversion results also depend on the numbers of inner and outer iterations: their tradeoff determines how often shaping regularization is applied and therefore controls its strength. Regularization by early stopping can also be conducted. The optimization strategy with $\mathbf{H}_{\epsilon,N,K}$ removed corresponds to the iterative thresholding approach (Daubechies et al., 2004).

Workflow

The workflow takes stacked data as the input. To generate all the inputs necessary for the inversion we propose the following sequence of procedures:

1. estimate inline and crossline dips describing dominant local slopes associated with reflections in the stack;
2. perform PWD filtering on the stack in inline and crossline directions;
3. migrate the corresponding volumes;
4. combine the migrated volumes in a structure tensor (equation 2);
5. smooth structure tensor components along structures with edge preservation;
6. perform eigendecomposition of a structure tensor and determine orientations of edges;
7. apply AzPWD and path-summation integral to the stacked data;
8. apply conventional full-wavefield migration to the dataset stack (same as the input to step 1); estimate dips and generate PWD volumes in the inline and in the crossline directions in the image domain ($\mathbf{D}_{\text{im}}$ in equation 3) for anisotropic smoothing regularization.

The sequence of procedures with their corresponding inputs and outputs is shown in Figure 2. In the first step, dips are estimated using PWD (Fomel et al., 2007), and two volumes - one for the inline dips and one for the crossline dips - are produced and further used for reflection removal in step 2. In the second step, based on the two input dip volumes, reflections are predicted and suppressed: two outputs are generated, which correspond to PWD filter application in the inline ($\mathbf{D}_x$) and in the crossline ($\mathbf{D}_y$) directions using the corresponding dip distributions. These two volumes with reflections removed are then migrated (step 3) using conventional full-wavefield migration, e.g. 3D post-stack Kirchhoff migration. For step 4, instead of explicitly computing structure tensor for each data sample according to equation 2, volumes for each of its components can be pre-computed. The term $p_x p_x$ structure-tensor component volume can be generated by the Hadamard product between the migrated inline PWD volume ($\mathbf{P}_x$) and itself, the $p_y p_y$-component volume - by the Hadamard product between the migrated crossline PWD volume ($\mathbf{P}_y$) and itself, and the $p_x p_y$-component volume - by the Hadamard product between the migrated inline PWD volume ($\mathbf{P}_x$) and the migrated crossline PWD volume ($\mathbf{P}_y$). Then, in step 5, the $p_x p_x$, $p_y p_y$, and $p_x p_y$ structure-tensor component volumes are input to edge preserving smoothing, which outputs the $\langle p_x p_x \rangle$, $\langle p_y p_y \rangle$, and $\langle p_y p_y \rangle$ volumes. In step 6, structure tensor (equation 2) eigendecomposition is performed "on the fly" by combining structure tensor component values from the $\langle p_x p_x \rangle$, $\langle p_y p_y \rangle$, and $\langle p_y p_y \rangle$ volumes for each data sample. The result is the smaller eigenvalue eigenvector volume, which is then converted to edge diffraction orientations $\mathbf{\Theta}$. Step 7 gives the data to be fit by the inversion (equation 1). Orientations of structures for AzPWD and for anisotropic smoothing regularization are estimated in step 6. In anisotropic diffusion instead of derivatives in Cartesian coordinates we use PWDs in inline and crossline directions in the image domain ($\mathbf{D}_{\text{im}}$ in equation 3), dip estimation for which should be performed on a "conventional" image of a full wavefield stack (step 8). Then, we invert the data for edge diffractions.

SYNTHETIC DATA EXAMPLE

We test the approach on a synthetic data example with a reflectivity model is shown in Figure 3. The synthetic seismic data are generated by Kirchhoff modeling method with 15 Hz peak-frequency Ricker wavelet, reflectivity distribution shown in Figure 3 and 2.0 km/s constant velocity model, which is further utilized in both migration and inversion. Zero-offset geometry with 1 m sampling in both inline and crossline directions is used. The synthetic data are shown in Figure 4a. Random noise with a maximum amplitude of 30% of that of the signal, filtered to the signal frequency band is added to the synthetic. After 3D Kirchhoff migration diffractions become focused and a channel-like structure with a zigzag pattern becomes prominent (Figure 4b). However, channel edges appear to be somewhat blurred and masked by the reflections. We follow the workflow described above. Data to be fit by the inversion is shown in Figure 5a. We use the following parameters for the inversion: $\lambda = 100$, $\epsilon = 10$, $N = 5$ and $K = 1$. In total we use 20 iterations - 5 inner by 4 outer. The inversion result is shown in Figure 5b. Edges are highlighted and denoised.

FIELD DATA EXAMPLE I

We test the capabilities of the proposed approach on the field dataset acquired with a high-resolution 3D (HR3D) marine seismic acquisition system (P-cable) in the Gulf of Mexico to characterize structure and stratigraphy of the shallow subsurface (Meckel and Mulcahy, 2016; Klokov et al., 2017b; Merzlikin et al., 2017b; Greer and Fomel, 2018). The acquisition geometry is defined by a 'cross cable' of a catenary shape

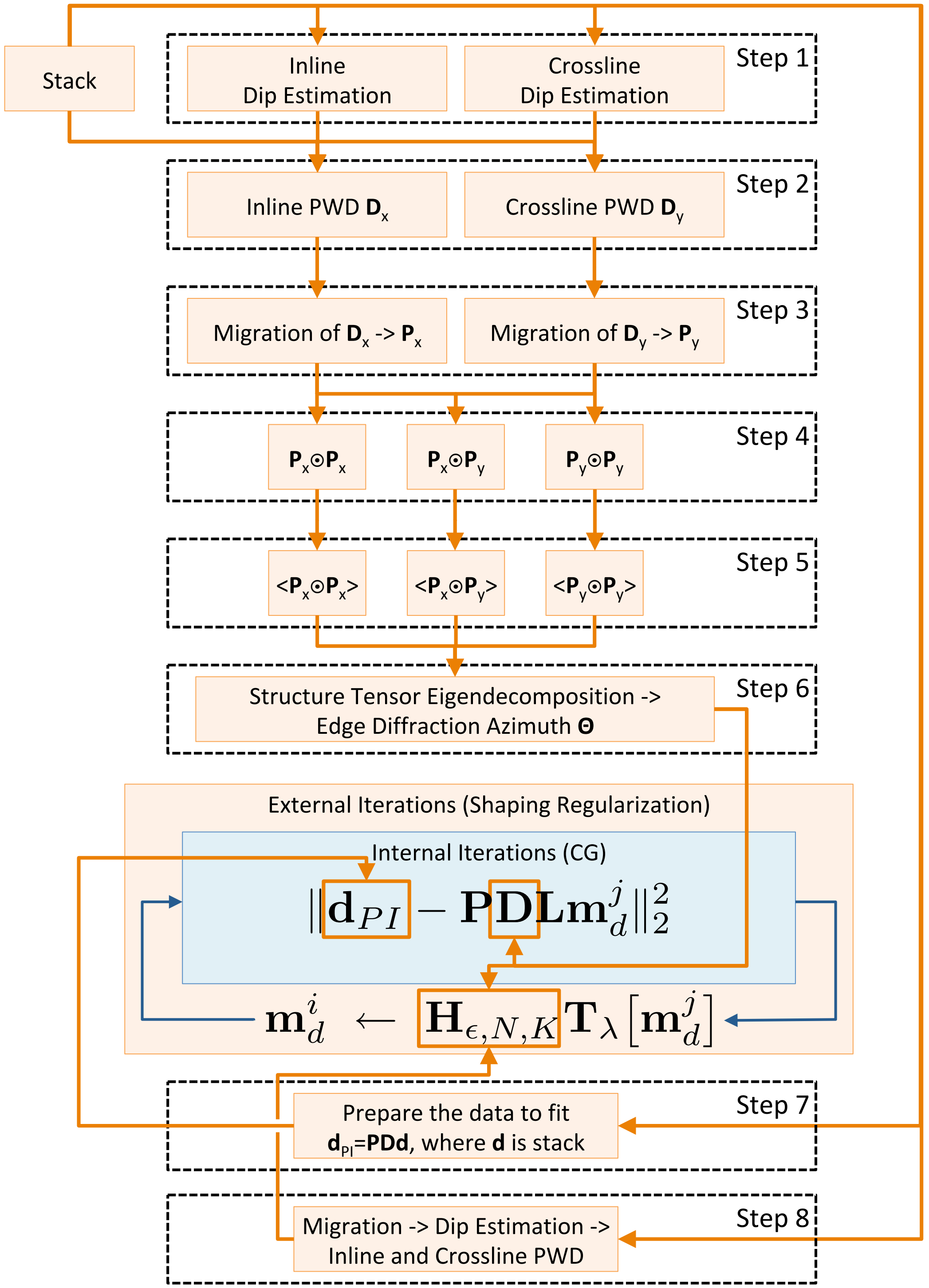

Figure 2: Workflow chart illustrating the sequence of procedures and the relation of their corresponding inputs and outputs. Here, $\mathbf{D}_x$ and $\mathbf{D}_y$ correspond to inline and crossline PWD volumes of the input stack, $\mathbf{P}_x$ and $\mathbf{P}_y$ correspond to inline and crossline PWD volumes after migration, $\odot$ corresponds to the Hadamard (element-wise) matrix product, $\langle\rangle$ corresponds to the edge-preserved smoothing, $\mathbf{\Theta}$ corresponds to the volume of edge diffraction azimuths, $\mathbf{PDL}$ corresponds to the forward modeling operator corresponding to the chain of path-summation integral, AzPWD and Kirchhoff modeling operators respectively; $\mathbf{d}_{PI} = \mathbf{PDd}$, where $\mathbf{d}$ corresponds to the input stack; and $\mathbf{H}_\epsilon$ and $\mathbf{T}_\lambda$ are anisotropic-smoothing and thresholding operators. The term $\mathbf{m}_d$ is the edge diffractivity we invert for: $\mathbf{m}_d^j$ describes model updates from internal iterations minimizing the misfit, and $\mathbf{m}_d^i$ is the result of regularization applied

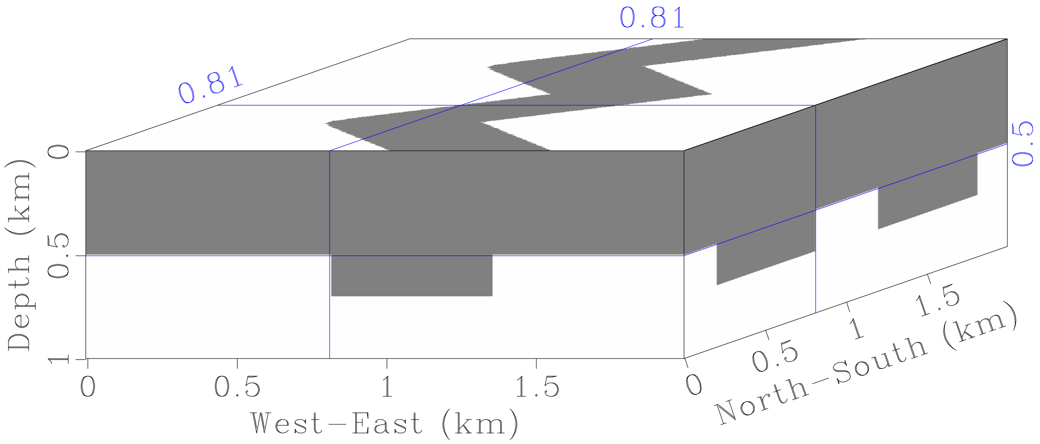

Figure 3: Reflectivity model for the synthetic data example. Reflectivity corresponds to density contrasts while the velocity is kept constant at 2.0 km/s throughout the volume.

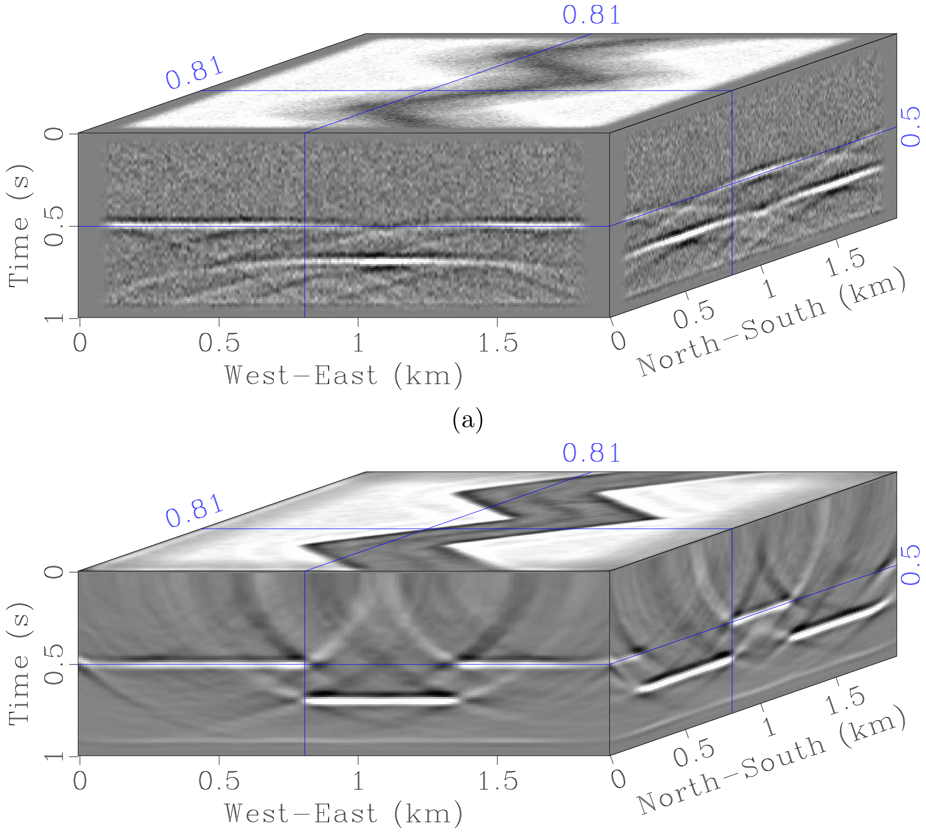

(a)

(b)

Figure 4: (a) Zigzag zero-offset synthetic; (b) 3D Kirchhoff time migration of the zigzag zero-offset synthetic (Figure 4a). While focusing of both reflections and edge diffractions can be observed in (b), channel edges are masked by specular energy and appear to be blurred.

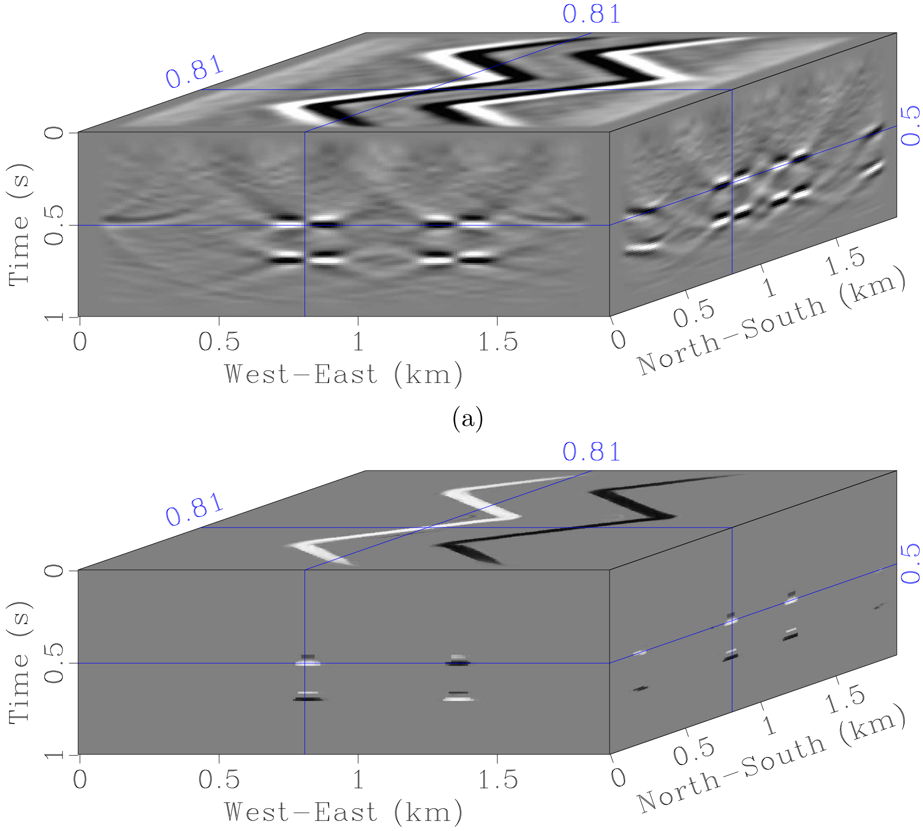

(a)

(b)

Figure 5: (a) AzPWD and path-summation integral migration applied to the zigzag zero-offset synthetic (Figure 4a) : A high diffraction probability along the channel edges can be observed; (b) Inversion result: edge diffractions are highlighted and denoised.

with paravans (diverters) at the ends oriented perpendicular to the inline (transit) direction that tows twelve 25 m long streamers with separation of $10 - 15$ m. Source-receiver offsets are on order of $100 - 150$ m, while the source sampling is 6.25 m. The target interval of interest in this paper is associated with the 0.222 s time slice, which approximately corresponds to 160 m depth. Diffraction imaging is applied to the dataset stack preprocessed with the following procedures: 40 Hz low-pass filter, wavelet deconvolution, surface-consistent amplitude corrections, predictive deconvolution, missing trace interpolation and acquisition footprint elimination using F-K filtering in the image domain. More detailed description of the acquisition geometry, geology, and interpretation of diffraction images can be found in Klokov et al. (2017b) and Merzlikin et al. (2017b). Here we focus on the interval with a channel of high wavelength sinuosity (Merzlikin et al., 2017b). For simplicity, constant velocity model of 1.5 km/s is used for both migration and inversion. Higher accuracy diffraction-based velocity estimation for the same dataset is described in Merzlikin et al. (2017b).

The stacked volume is shown in Figure 6. The post-stack 3D Kirchhoff time migration image of the target slice is shown in Figure 7a. Channel delineation is hindered by stronger reflections and acquisition footprint - horizontal lines. We eliminate the footprint in inline and crossline PWD diffraction images using F-K filtering before combining them in a structure tensor (equation 2) and forming AzPWD linear combination (Merzlikin et al., 2017b). Result of AzPWD volume migration is shown in Figure 7b. Channel and other small-scale features (e.g. fault at in-lines $2.5 - 3.0$ km and cross-lines $6.0 - 6.4$ km) are highlighted but the image is still noisy.

We follow the proposed workflow and first generate the data to be fit by the inversion (Figure 8a) by applying AzPWD and path-summation integral migration to the stack (Figure 6). We run five outer and two inner iterations and use $\lambda = 0.008$, $\epsilon = 20$, $N = 30$ and $K = 1$. Due to low signal-to-noise ratio of the dataset small number of inner iterations is used to prevent leakage of noise to the diffraction image domain. The result of the proposed approach is shown in Figure 8b. The channel appears to be highlighted and denoised. Most of the low-amplitude events are also preserved and highlighted including the fault feature (in-lines $2.5 - 3.0$ km and cross-lines $6.0 - 6.4$ km). Discontinuities of edges intersecting each other at inlines $1.0 - 1.5$ km and crosslines $4.0 - 5.0$ km are caused by their rapidly varying orientations prohibiting smoothing from emphasizing different strikes simultaneously.

Figures 9a and 9b show the diffractivity model after thresholding and after thresholding followed by anisotropic smoothing applied correspondingly. The figures illustrate that anisotropic smoothing merges neighbor samples and thus is necessary for edge diffraction regularization. The result is consistent with the experiments shown in Figure 1.

Figure 10 shows the stack after reflection elimination, modeled diffractions from denoised diffractivity shown in Figure 8b and their difference. Denoised diffractions in Figure 10b show clear hyperbolic signatures. Reflection energy remainders after AzPWD application prominent in Figure 10a (e.g., 0.222 s TWTT (two-way trav-

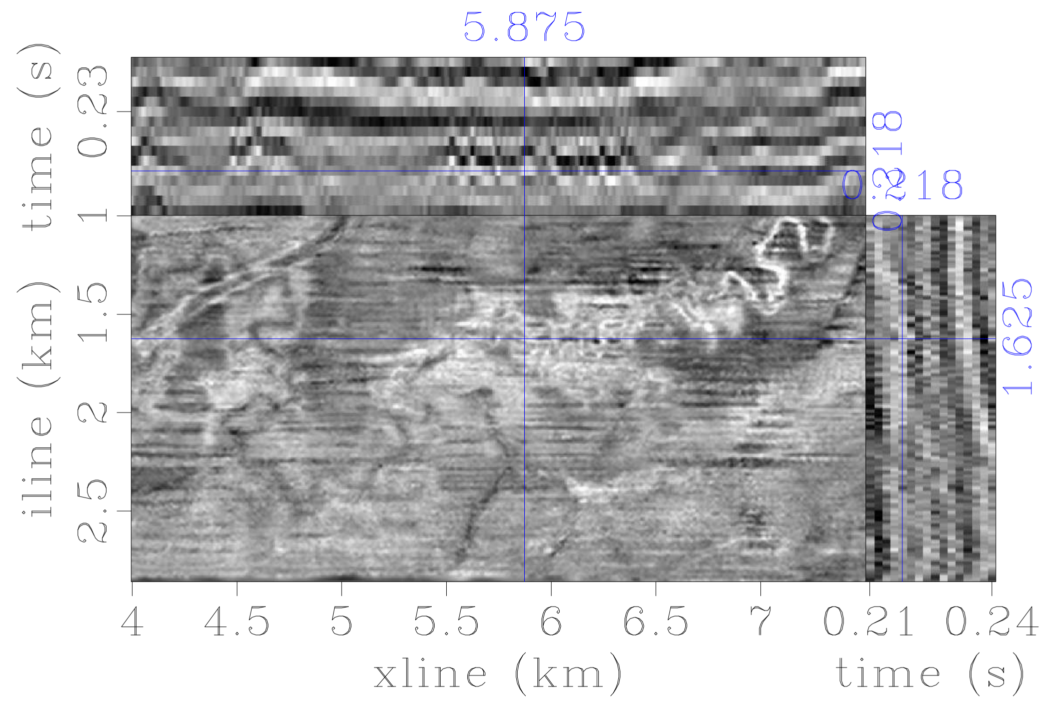

Figure 6: High-resolution 3D marine seismic dataset from the Gulf of Mexico: stacked volume.

eltime), inline 1.625 km and crosslines 5.5 − 6.25 km and 0.222 s TWTT, inlines 2.4 − 2.7 km and crosslines 6.25 − 6.5 km) are also removed. Difference in Figure 10c is predominated by noise, reflection remainders (e.g., regions mentioned above) and acquisition footprint and proves the effectiveness of the approach.

To account for amplitude differences and for higher continuity of denoised diffractions (Figure 10b) in comparison to the stack with AzPWD (Figure 10a) signal and noise orthogonolization (Chen and Fomel, 2015) has been applied. Similarity between restored signal (Figure 10b) and restored noise (Figure 10c) is measured. Then, signal energy, which leaked to the difference volume (Figure 10c) and which has high similarity with the signal events actually predicted (Figure 10b), is withdrawn from the noise volume and added to the signal estimate.

FIELD DATA EXAMPLE II

The second field data example comes from the Cooper Basin onshore Western Australia. The dataset corresponds to stacked (with 25 × 25 m bin size) preprocessed data acquired as a 3D land seismic survey with fully azimuthal distribution of offsets and a far offset of 4000 m. Preprocessing sequence includes noise attenuation, near-surface static corrections, despike, surface-consistent deconvolution, Q-compensation whitening and time-variant filter applied after stacking. The target horizon slice picked by

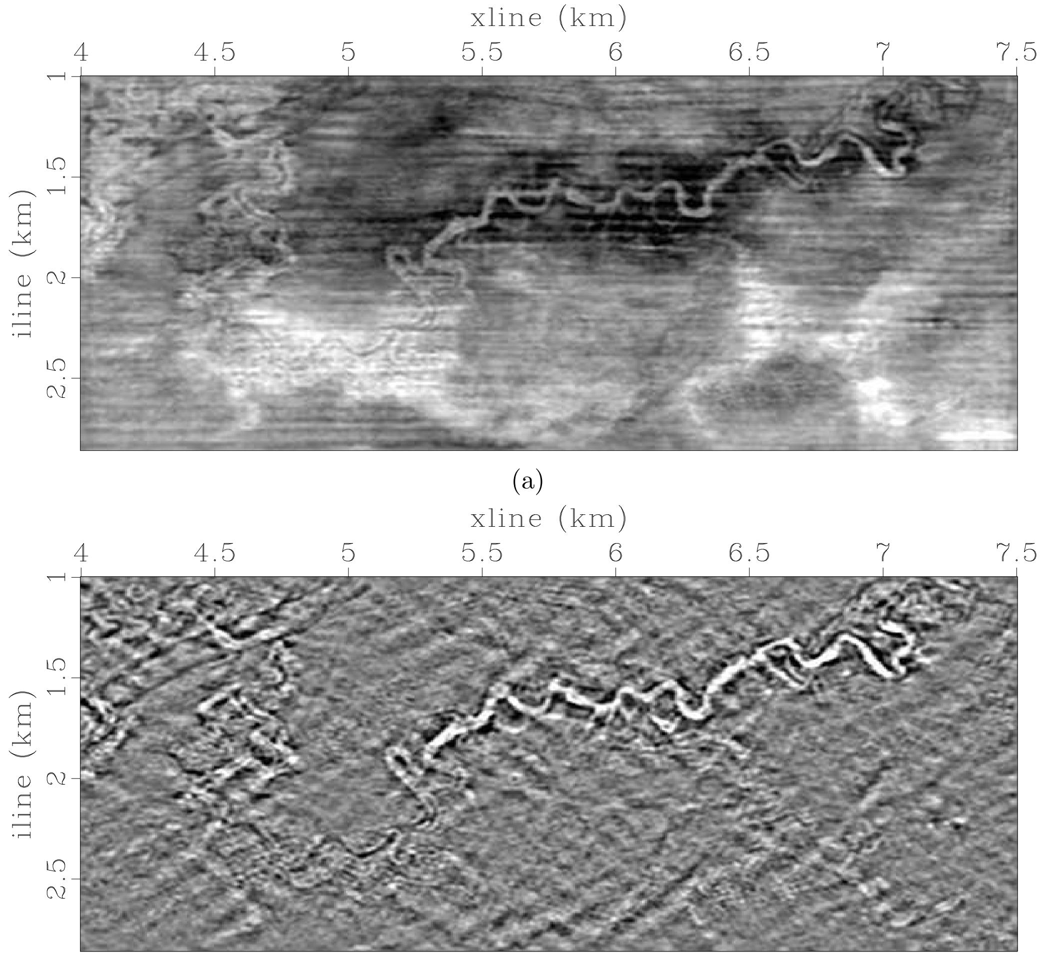

(a)

(b)

Figure 7: 0.222 s time slice: (a) 3D post-stack Kirchhoff migration of the stack shown in Figure 6; (b) 3D post-stack Kirchhoff migration of the stack after AzPWD. Subsurface discontinuities appear to be highlighted in (b) in comparison to (a), in which they are masked by specular energy. At the same time, diffraction image (b) still appears to be noisy.

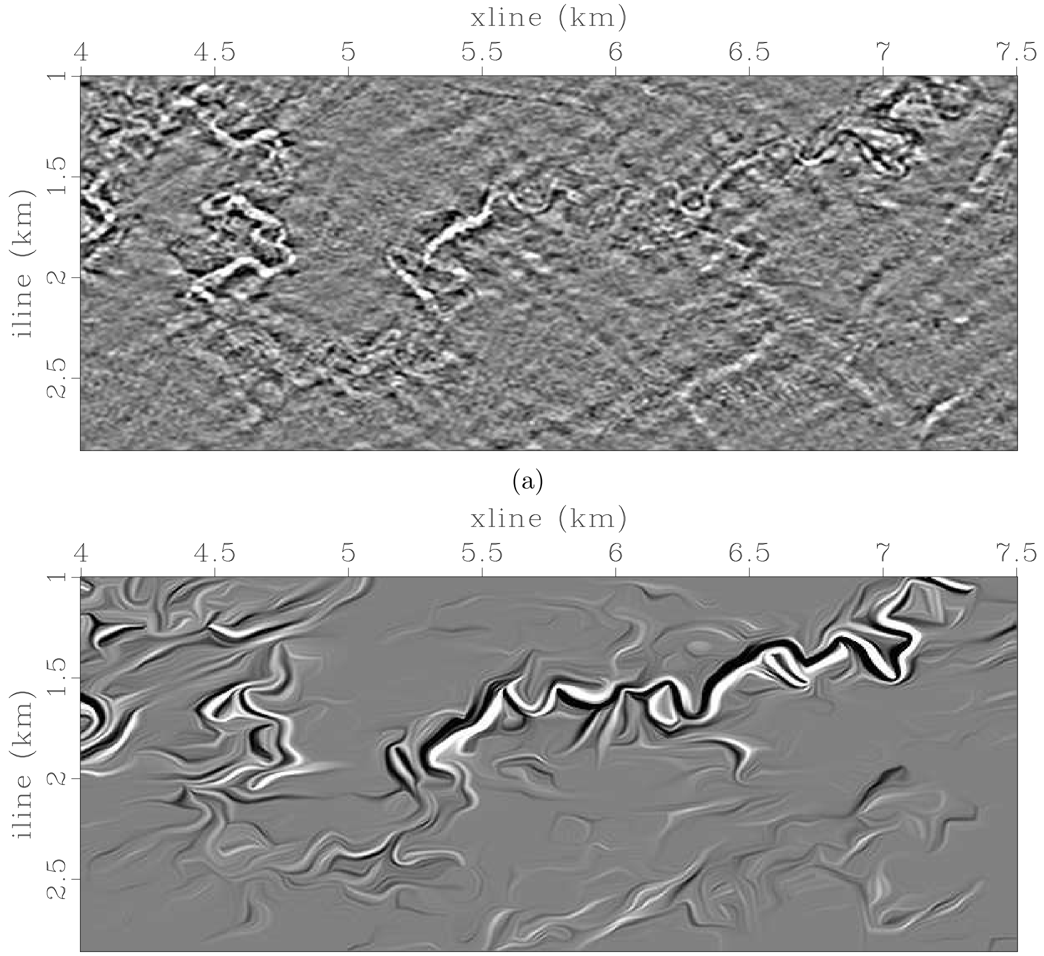

(a)

(b)

Figure 8: 0.222 s time slice: (a) observed data (Figure 6) preconditioned by AzPWD and path-summation integral migration; (b) inversion result (strong smoothing is used to highlight the continuity of edge diffractions). Significant improvement in signal-to-noise ratio of edge diffractions has been achieved (compare with Figure 7b).

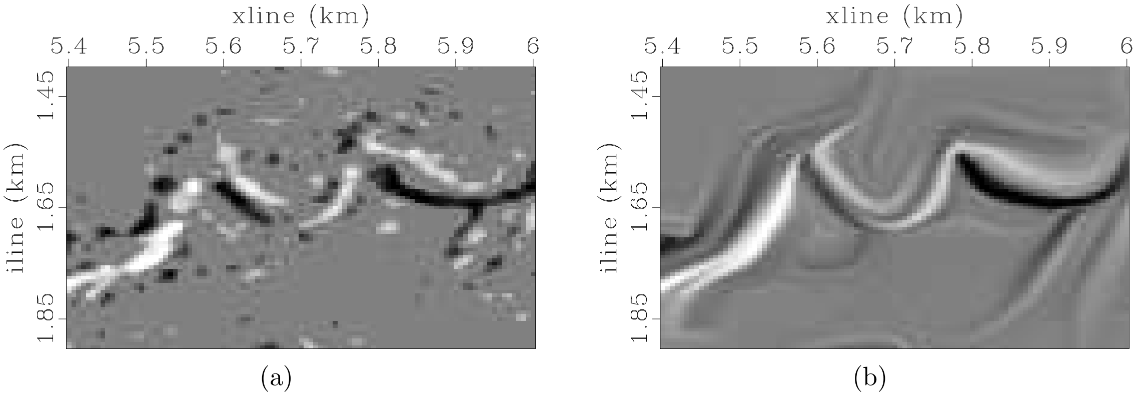

(a) (b)

Figure 9: Last iteration diffractivity model: (a) after thresholding; (b) after thresholding followed by anisotropic smoothing. While thresholding allows for denoising, anisotropic smoothing emphasizes edge diffraction continuity and accounts for its kinematic behavior when observed along the edge.

the interpreter and used for the performance evaluation of the method corresponds to the interface between tight-gas sand and coals (Tyiasning et al., 2016). The depth of the interface is approximately 2500 m. Structural complexity of the overburden can be characterized as high. Detailed geological description of the area as well as the comparison of diffraction imaging results to discontinuity-type attributes is given by Tyiasning et al. (2016). Here, we apply the developed approach to the dataset. Prestack time migration velocity is used for both full-wavefield migration and the proposed inversion approach for edge diffraction imaging.

Figure 11 shows a stacked volume of the dataset. We focus on the window around the target horizon, which on average corresponds to 1.72 s TWTT. Figure 12a shows conventional image of the target horizon slice generated with 3D post-stack time Kirchhoff migration. We then apply reflection removal procedure to the stack (Figure 11), migrate it, and generate the image shown in Figure 12b. Smaller scale features become highlighted, e.g., faults between $8-10$ km inlines and $0-4$ km crosslines. Acquisition footprint is noticeable on both of the images (Figure 12) and corresponds to the low-amplitude events aligned in a grid-like fashion (easy to notice between inlines $0-2$ km and crosslines $6-8$ km). We apply the developed workflow to further highlight and denoise diffractions.

First, we generate the data to be fit by the inversion - the stack weighted by a path-summation integral after reflection elimination (Figure 13a). We run twenty outer and two inner iterations and use $\lambda = 4$, $\epsilon = 10$, $N = 20$ and $K = 1$. As in the previous data example we use a low number of internal iterations to avoid noise fitting in general and footprint in particular. The inversion result along the target horizon is shown in Figure 13b. 3D cubes of the migrated stack, the migrated stack after reflection elimination and the inversion result are shown in Figures 14, 15 and 16. Edges masked by the specular energy on the full-wavefield image (Figure 14), are

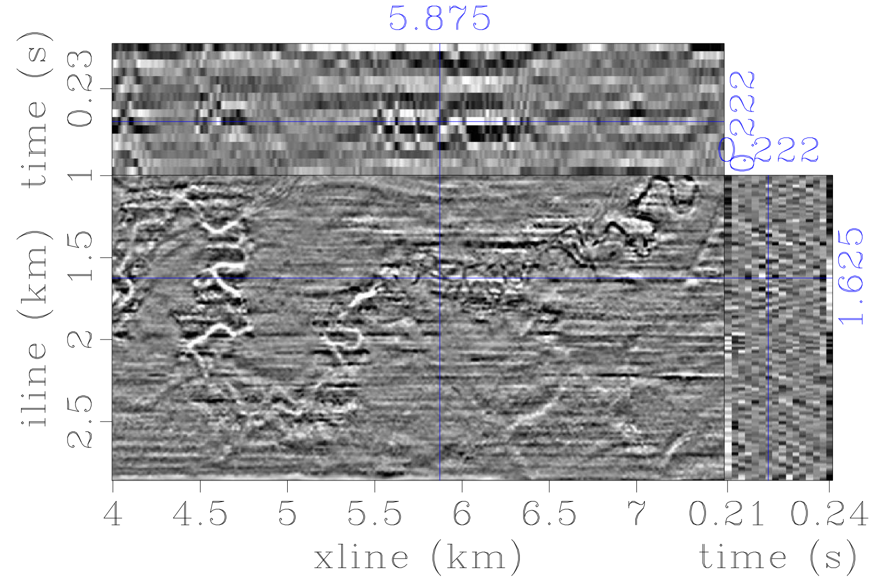
5.875
time (s)
0.23
1
iline (km)
1.5
2
2.5
0.222
0.222
1.625
4
4.5
5
5.5
6
6.5
7
0.21
0.24
xline (km)
time (s)

(a)

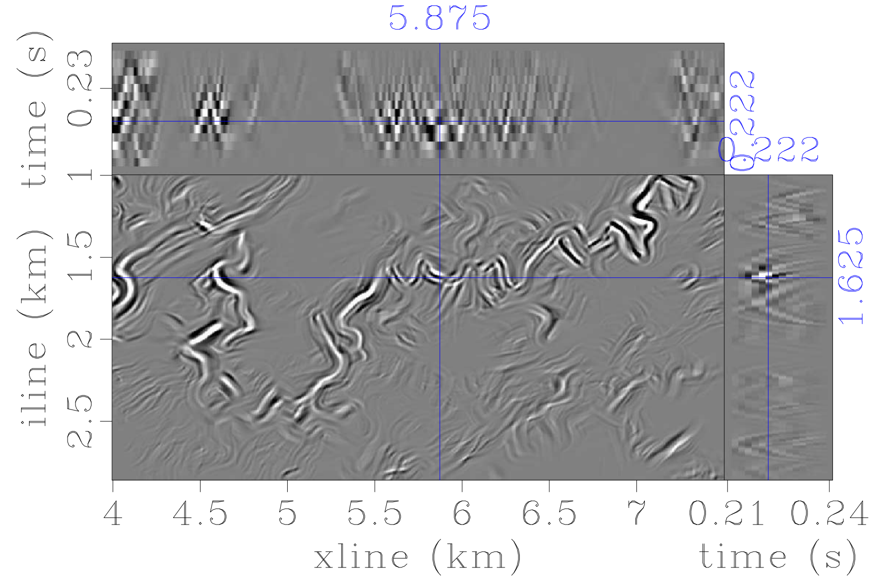
5.875
time (s)
0.23
1
iline (km)
1.5
2
2.5
0.222
0.222
1.625
4
4.5
5
5.5
6
6.5
7
0.21
0.24
xline (km)
time (s)

(b)

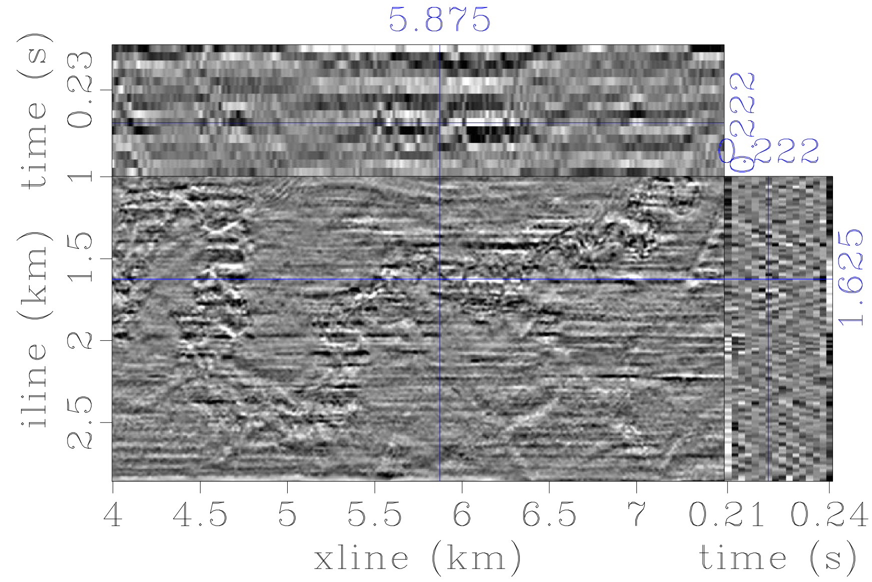
5.875
time (s)
0.23
1
iline (km)
1.5
2
2.5
0.222
0.222
1.625
4
4.5
5
5.5
6
6.5
7
0.21
0.24
xline (km)
time (s)

(c)

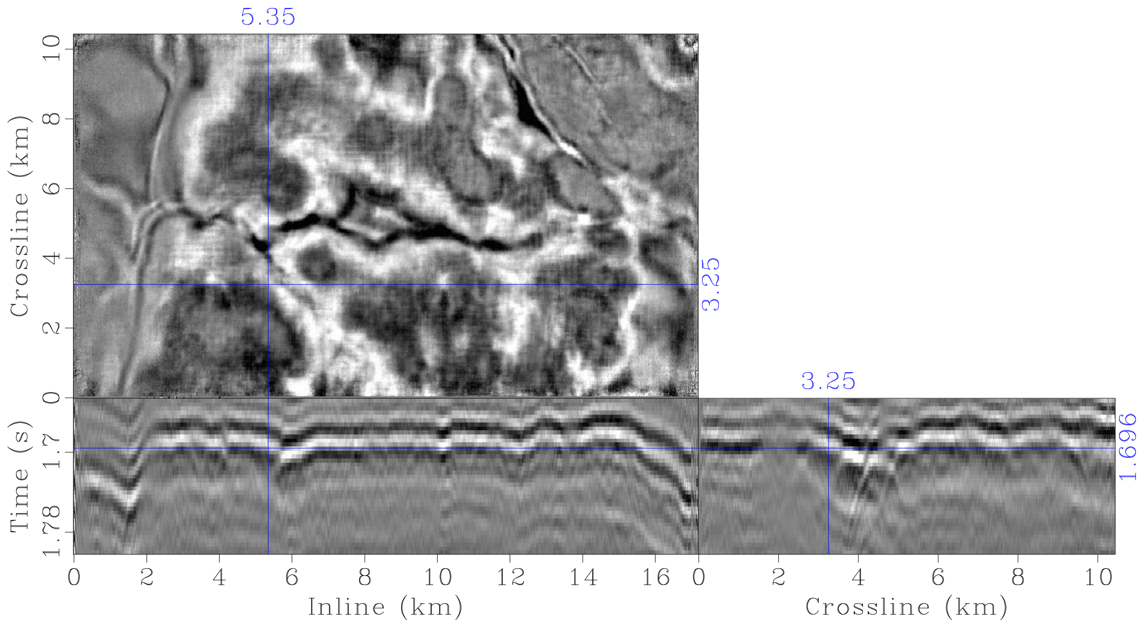

Figure 11: 3D sesimic dataset from the Cooper Basin onshore Western Australia: stacked volume.

highlighted on the image after reflection elimination (Figure 15). At the same time, edge diffractions produced by the inversion (Figure 16) appear to be clearer and have higher signal-to-noise ratio.

Further, we apply Kirchhoff modeling to the inversion result (Figures 13b and 16), restore diffractions (Figure 17), and subtract the result from the stack after reflection elimination (Figure 18). The result of subtraction shown in Figure 19 can be treated as noise eliminated during the inversion. Signal and noise orthogonalization (Chen and Fomel, 2015) is applied to account for aperture difference between observed and restored diffractions (for instance, often only a single diffraction flank can be observed in the data leading to spuriously high difference or the “noise estimate”) and to bring back some of the energy accidentally leaked to the noise domain.

The acquisition footprint evident in Figure 19 suggests the high performance of the method. Improvement can be noticed between $6-10$ km inlines and $2-4$ km crosslines associated with the extraction of small-scale discontinuities. Compare the inversion result Figure 13b and the result of migration shown in Figure 12b. Same subtle events are located at crossline 3.25 km between inlines $7-9$ km (Figures 17 and 18) and have a clear hyperbolic shape (Figure 17), which appears when edge diffractions are observed perpendicular to edges. Good restoration quality can also be inferred from the “circular” structure between $6-8$ km inlines and $0-2$ km crosslines. Both of these areas have high similarity between the initial diffraction stack (Figure 18) and the stack with diffractions “restored” and denoised by inversion (Figure 17) leading to low amplitudes in the difference section (Figure 19) primarily associated with noise.

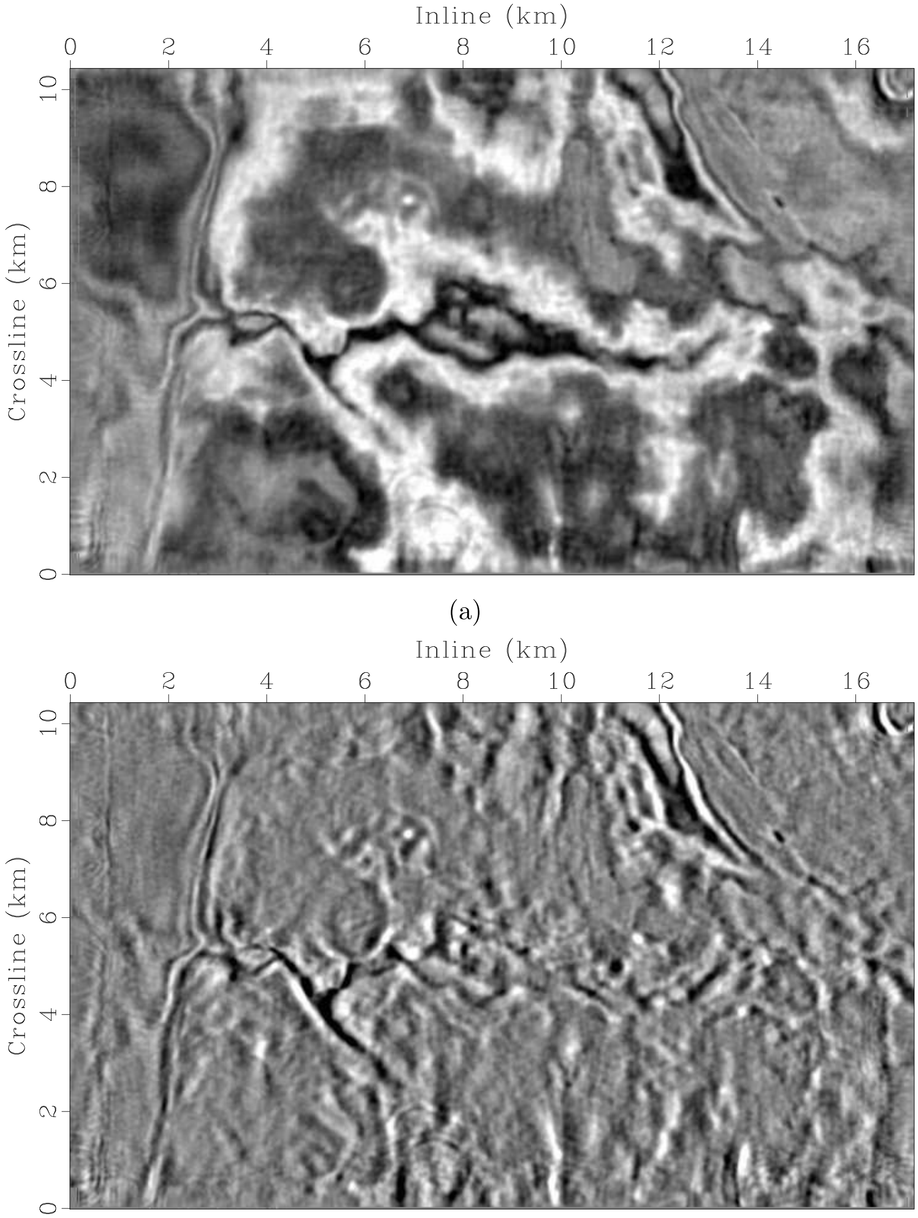

(a)

(b)

Figure 12: Target horizon slice (the interface between tight-gas sand and coals picked by the interpreter ($\sim$ 1.72 s TWTT)): (a) 3D post-stack Kirchhoff migration of the stack shown in Figure 11; (b) 3D post-stack Kirchhoff migration of the stack after AzPWD. Subsurface discontinuities appear to be highlighted in (b) in comparison to (a), in which they are masked by specular energy. At the same time, diffraction image (b) still has some noise present.

These features also follow "frowning"-focusing-"smiling" behaviour under migration velocity perturbation supporting their diffraction nature in the plane perpendicular to the edge.

Some features are lost in the area between $10 - 11$ km inlines and $6 - 8$ km crosslines. Event between inlines $12 - 14$ km and crosslines $6 - 8$ km is not predicted (Figure 19). High magnitude events observed between inlines $1 - 3$ km at crossline 3.25 km and between crosslines $4 - 5$ km at inline 5.35 km (Figure 16 and 17) can be associated with reflections leaked to the diffraction image domain or can actually be edge diffractions observed in the plane not perpendicular to the edge and thus having elongated signature. The event located at crossline 3.25 km between inlines $5 - 7$ km inversion interprets as a reflection and removes it from the diffraction imaging result (Figure 16 and 17). High difference values following the channel in the difference cube (Figure 19) can also be associated with the reflection remainders removed from the diffraction image domain.

It should be mentioned that the target horizon has a highly oscillating pattern including a high magnitude drop in the left part of the cube (inlines $1-3$ km) making dip estimation for "ideal" reflection-diffraction separation simultaneously for the whole area challenging. More careful dip estimation possibly with different parameters in different regions of the dataset should further improve the result. Inversion parameters can definitely be tweaked to improve the results but even with these trial values the majority of the edges including some subtle features (e.g., events at crossline 3.25 km between inlines $7 - 9$ km (Figure 16)) hardly noticeable on the migrated stack after reflection elimination (Figure 15) has been extracted and highlighted.

DISCUSSION

The dependency of workflow's ability to produce sharp images of edge diffractions upon the migration velocity accuracy requires further investigation. On one hand, the approach incorporates least-squares migration framework known to be quite sensitive towards velocity model (Nemeth et al., 1999). On the other hand, path-summation integral provides a velocity-model-independent weighting of the misfit, which is expected to increase the method's tolerance towards velocity model errors.

The second field example illustrates the efficiency of the proposed approach in a complex geological environment. Most edge diffractions, and especially those associated with major discontinuities, are extracted and denoised. Some reflection energy remainders are present but are limited to locations characterized by a peculiar reflection pattern, which was not picked up by the dip estimation tuned to perform reflection-diffraction separation over the whole area. This is the dip estimation problem, results of which can be improved, for instance, by subdividing the area into smaller fragments, and, thus, does not question the validity of the approach presented. The latter statement is also supported by the high performance of the developed approach when applied to the first field data example. First field data

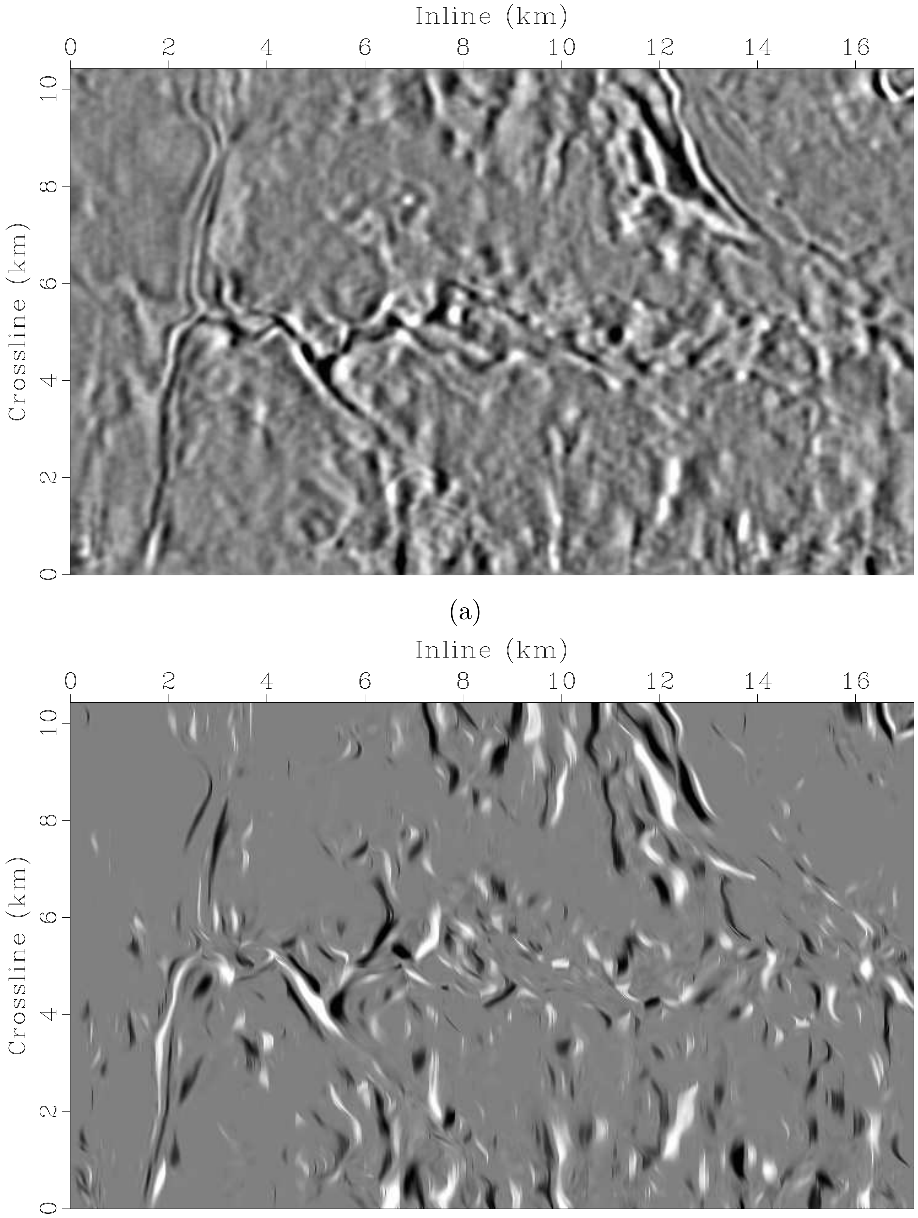

Figure 13: Target horizon slice (the interface between tight-gas sand and coals picked by the interpreter (~ 1.72 s TWTT)): (a) observed data (Figure 11) preconditioned by AzPWD and path-summation integral migration; (b) inversion result: edge diffractions have been denoised (compare with Figure 12b).

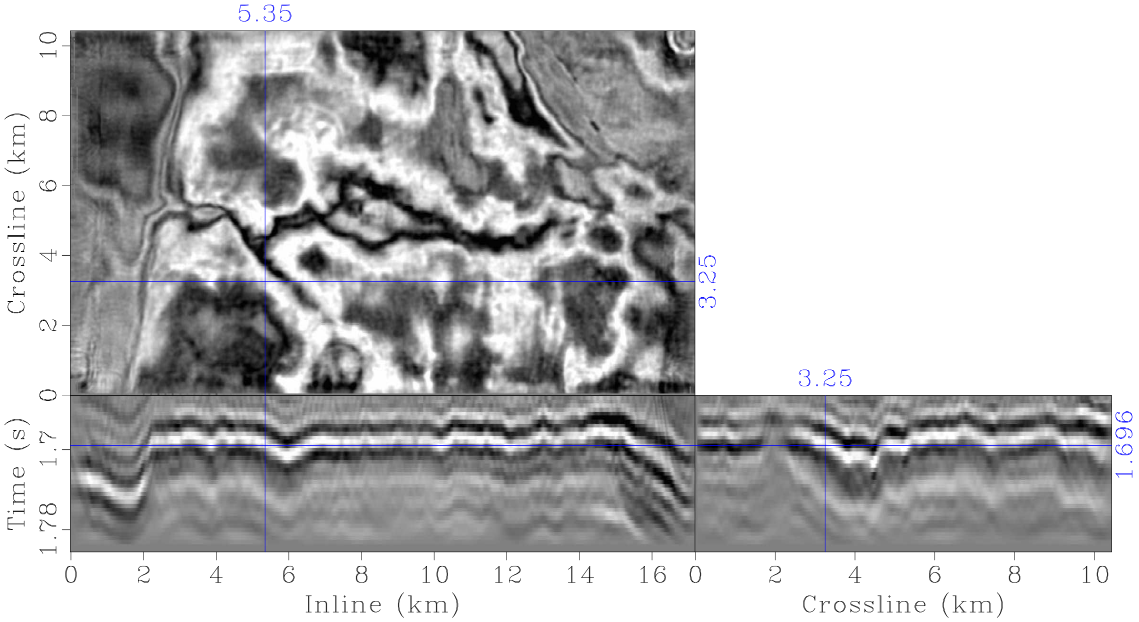

Figure 14: 3D post-stack Kirchhoff migration of the stack shown in Figure 11.

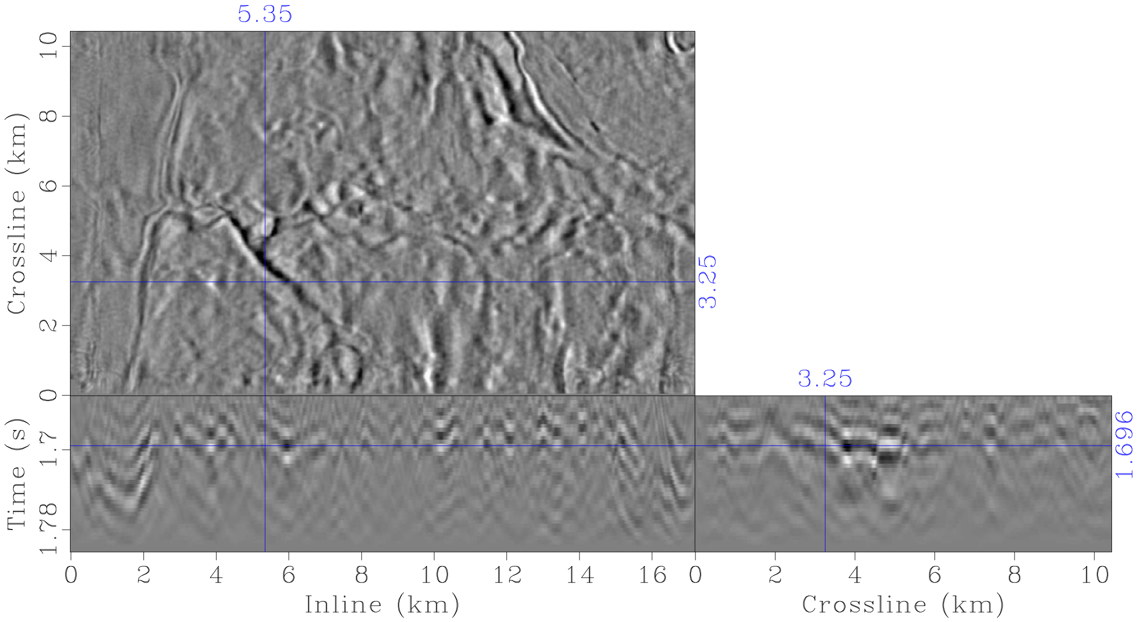

Figure 15: 3D post-stack Kirchhoff migration of the stack (Figure 11) after reflection elimination and edge diffraction extraction with AzPWD. Subsurface discontinuities appear to be highlighted in comparison to Figure 14, in which they are masked by specular energy. At the same time, diffraction image still has some noise present.

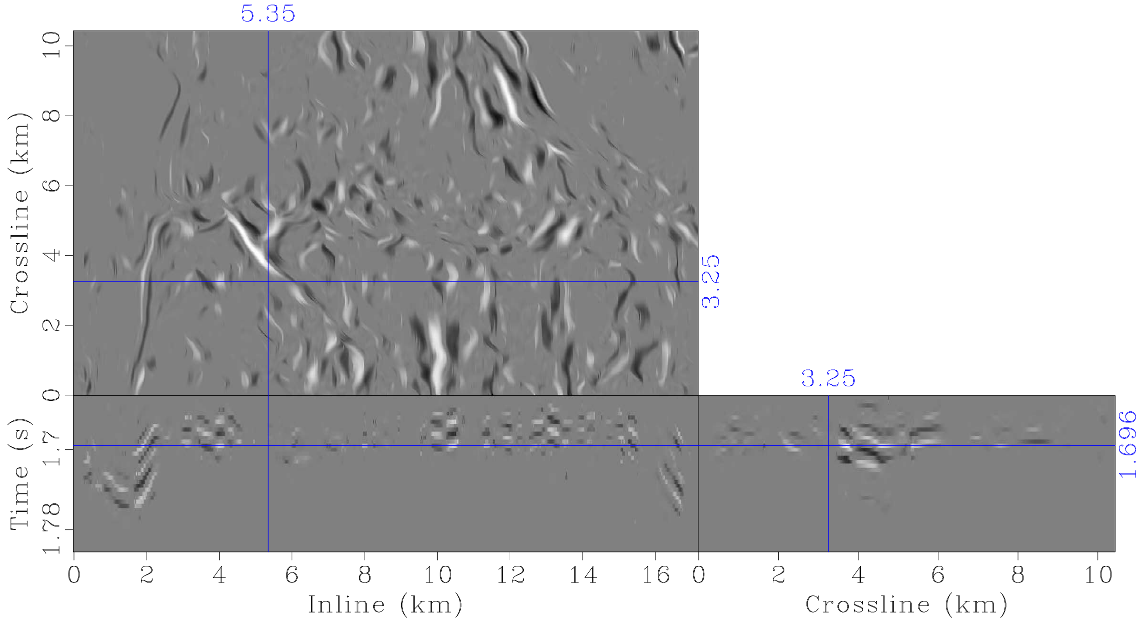

Figure 16: Inversion result. Edge diffractions are both highlighted and denoised (compare with Figure 15).

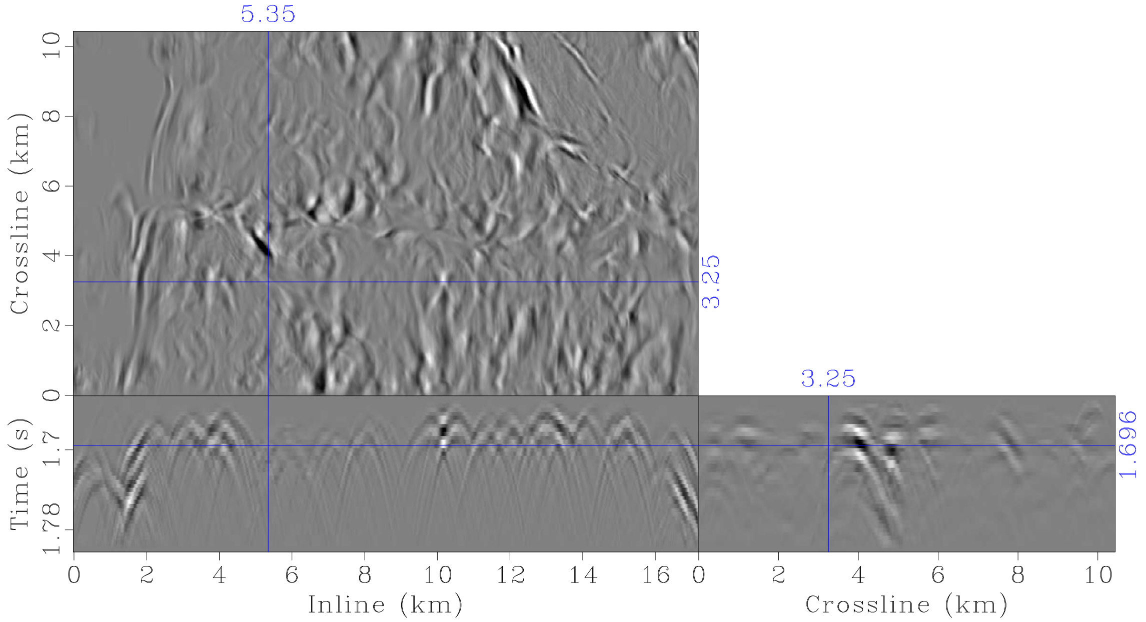

Figure 17: Kirchhoff modeling of diffractivity from Figure 16. “Clean” diffraction signatures are recovered: notice hyperbolic shapes when edge diffractions are observed perpendicular to edges.

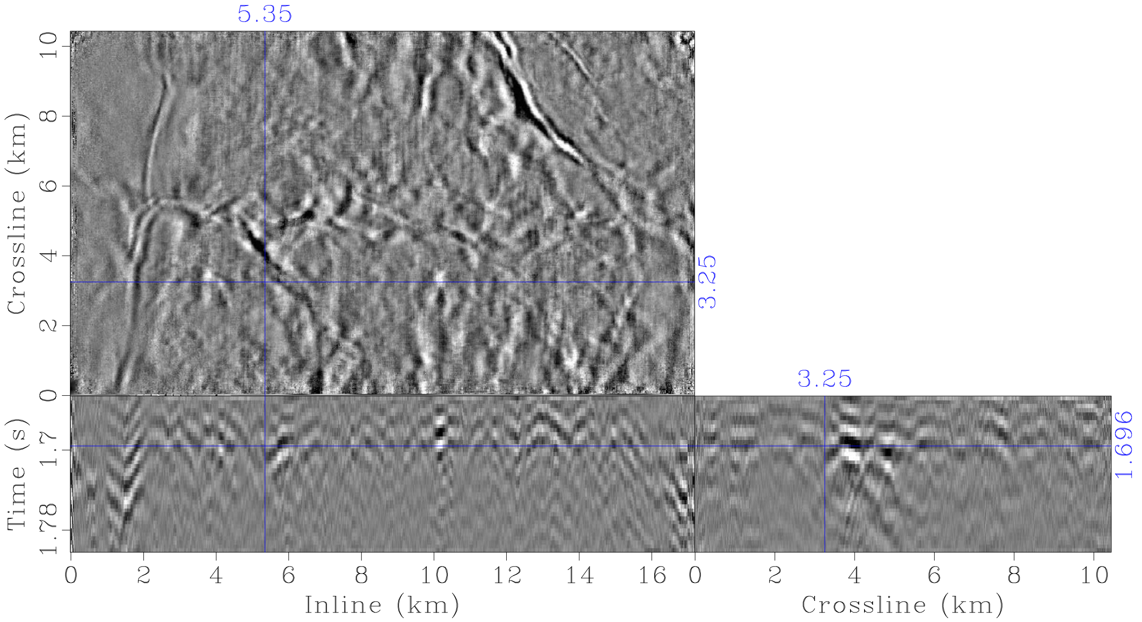

Figure 18: Stack with reflections removed. The majority of reflections is removed, some hyperbolic signatures can be seen (compare with Figures 11 and 17). Reflection remainders and noise including acquisition footprint are apparent (compare with Figure 17).

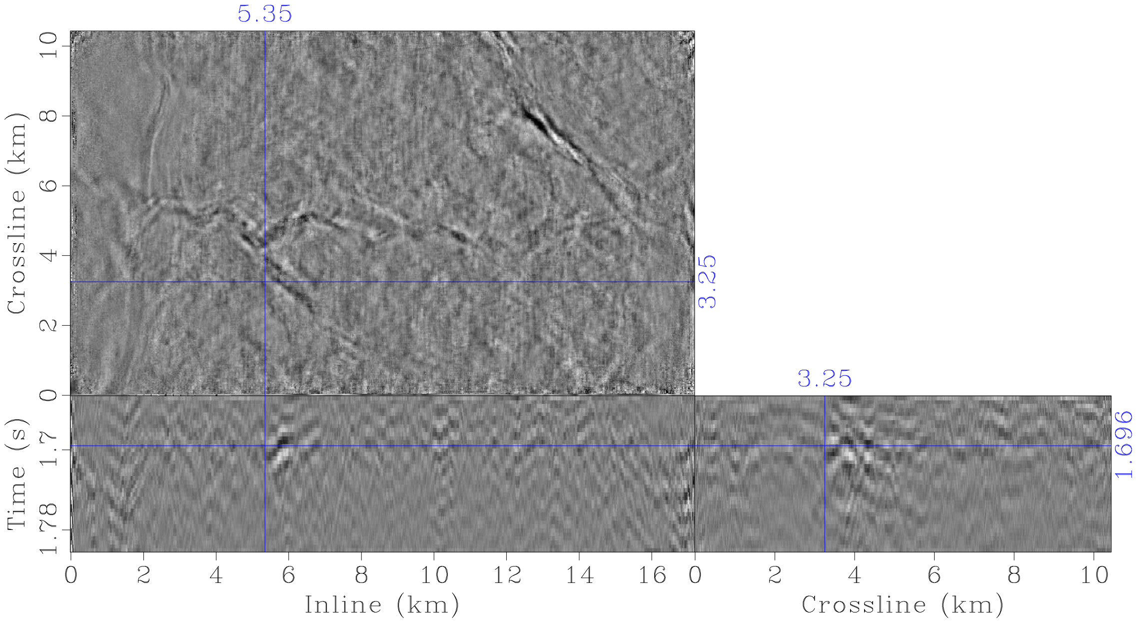

Figure 19: Difference between Figures 17 and 18 is predominated by noise and thus supports the validity of denoised edge diffractions (Figure 17).

example is characterized by a low signal-to-noise ratio and is highly contaminated by the acquisition footprint. The approach allows successfully untangling edge diffractions from reflections and noise and provides high resolution images of subsurface discontinuities. We expect that in production-like environment, geological knowledge can be used to further adjust the parameter values. For instance, in the first field data example expected channel sinuosity could guide the smoothing strength for the edges. In this paper, we focus on highlighting the advantages of the method rather than on delivering final results for drilling decisions.

The natural extension of the approach is to include reflection modeling into the inversion. As demonstrated by Merzlikin et al. (2019), both reflections and diffractions can be inverted for by the same forward modeling operator whereas the separation into the components can be done on the regularization level. Regularization of diffractions can stay the same whereas reflections, for instance, can be penalized by a strong isotropic smoothing operator along the dominant local slopes: specular events locally do not exhibit lateral symmetry as opposed to edges. Extension of the model space to include reflections can help to eliminate the reflection remainders in the diffraction image domain.

High complexity of the overburden often leads to the interference between seismic events, which results in the presence of multiple dominant local slopes at a single data sample. While, in this case, the effectiveness of the proposed inversion scheme in general and of AzPWD in particular will be degraded, the performance could be improved by pre-applying migration with approximate velocity model to untangle interfering events, running AzPWD, and then going back to the original data domain.

Anisotropic smoothing is capable of emphasizing one edge direction at once. Edges with conflicting orientations can be a challenge. The "brute force" way to tackle the challenge can be scanning for various edge diffraction orientations and picking the desired ones (Merzlikin et al., 2016). Then, inversion results with alternative orientations can be compared. At the same time, if coherent noise with a consistent spatial orientation is present in the data, it can be emphasized by anisotropic smoothing. Structure tensor orientation determination will treat this noise as signal. Poor illumination and velocity model errors can also reduce the accuracy of structure-tensor based edge diffraction orientation determination. The latter will degrade the performance of anisotropic-smoothing regularization operator. We expect the problem can be alleviated by utilizing a priori information about geologic discontinuities' orientation, e.g. by using predominant azimuths of the faults in the region extracted from a geomechanical model.

The workflow described in this paper is a 3D extension of the method proposed by Merzlikin and Fomel (2016). In two dimensions one cannot discriminate between point and edge diffractions. Distribution of scatterers is spiky and intermittent, which leads to a natural choice of sparsity constraints on the diffractivity model. The new inversion scheme is based on two regularization operators: thresholding and anisotropic smoothing. While thresholding operator imposing sparsity constraints applicable to both point and edge diffractions remains to be the same as in the 2D counterpart of the workflow, anisotropic smoothing enforces continuity along the directions picked up by the structure tensor and thus is only applicable to edge diffractions. Point diffractions, which are not elongated in space, will be smeared under anisotropic smoothing operator action. Currently, our method is biased towards edge diffractions.

Anisotropic smoothing can have spatially variable diffusion coefficient defining its strength (Weickert, 1998; Hale, 2009). For instance, the coefficient and the direction of smoothing can depend on the linearity, which can be computed as a ratio of eigenvalues of the PWD-based structure tensor and which can distinguish between the edges and regions of continuous amplitude variation (Hale, 2009; Wu, 2017). Spatially variable diffusion coefficient could help to alleviate smearing of point diffractions. Point diffractions in the diffractivity model will exhibit low linearity. For these samples smoothing power can be reduced and thresholding will be a predominant regularization operator.

The proposed approach is equivalent to total variation (TV) regularization (e.g., Strong and Chan (2003)), in which minimizing l_1 norm of a second derivative penalizes the model. Hessian of TV is guided by a structure tensor, which forces model smoothing to be applied along the edges with no smearing across them. Thus, TV regularization is similar to the one proposed in this paper and can also be used to penalize edge diffractions. TV implementation challenges are associated withregularization term differentiation during optimization. While this obstacle can be accommodated by using sophisticated optimization methods and representing l_1-norm as a square root with a damper (Chan et al., 1999; Burstedde and Ghattas, 2009; Anagaw and Sacchi, 2012), shaping regularization by anisotropic diffusion appears to be a viable, simple to implement and fast to converge alternative with no approximations required. Anisotropic smoothing can be used to regularize full wavefield images in "conventional" least squares migration and even in iterative velocity-model building methods.

The workflow can be utilized to extract and denoise diffractions for their subsequent depth imaging. Alternatively, a depth imaging operator can replace Kirchhoff time migration in forward modeling to allow for depth-domain model conditioning, while misfit weighting by path-summation integral is still performed in time migration domain.

The inversion can be extended to pre-stack domain. In this case, pre-stack counterparts of the chained forward modeling operators should be used: pre-stack path-summation integral (Merzlikin and Fomel, 2017), pre-stack migration engine and pre-stack AzPWD. While expressions for the former two exist, AzPWD has not been applied in the pre-stack domain. The corresponding method can be derived based on the approach developed by Taner et al. (2006).

CONCLUSIONS

We have developed an efficient approach to highlight and denoise edge diffractions based on least-squares migration. The inverted operator corresponds to the chain of path-summation integral filter, AzPWD and Kirchhoff modeling operators. While the combination of path-summation integral filter and AzPWD emphasizes edge diffraction signatures in the data domain, thresholding and anisotropic smoothing precondition them in the model domain by denoising and enhancing their continuity. Both forward modeling and shaping regularization operators guide the inversion towards restoration of edge diffractions. Synthetic and field data examples show high fidelity of the approach.

The efficiency of the proposed inversion scheme comes from the workflow application in time post-stack domain and shaping regularization framework leading to fast convergence. The inversion scheme we propose can be thought of as an effective operator directly tailoring edge diffractions and extracting them from the full wavefield.

ACKNOWLEDGEMENTS

We are grateful to TCCS sponsors and in particular to Equinor (formerly Statoil) for financial support of this research. We thank Evgeny Landa, Andrej Bona, Timothy Meckel, Omar Ghattas and Luke Decker for inspiring discussions. We thank developers of and contributors to the Madagascar open source software project. We thank four anonymous reviewers, associate editors and Jeffrey Shragge for valuable comments and help in improving the manuscript. Pre-stack time migration velocity and preprocessed stack are provided by GeoFrac research consortium at the Australian School of Petroleum at the University of Adelaide.

REFERENCES

Alonaizi, F., R. Pevzner, A. Bona, V. Shulakova, and B. Gurevich, 2013, 3D diffraction imaging of linear features and its application to seismic monitoring: Geophysical Prospecting, **61**, 1206–1217.

Anagaw, A. Y., and M. D. Sacchi, 2012, Edge-preserving seismic imaging using the total variation method: Journal of Geophysics and Engineering, **9**, 138–146.

Berkovitch, A., I. Belfer, Y. Hassin, and E. Landa, 2009, Diffraction imaging by multifocusing: Geophysics, **74**, no. 6, WCA75–WCA81.

Bona, A., and R. Pevzner, 2015, Using Fresnel zone to characterise and image different types of diffractors in low S/N situations: Expanded Abstracts 77th EAGE International Conference, N116.

Burnett, W. A., A. Klokov, S. Fomel, R. Bansal, E. Liu, and T. Jenkinson, 2015, Seismic diffraction interpretation at Piceance Creek: Interpretation, **3**, no. 1, SF1–SF14.

Burstedde, C., and O. Ghattas, 2009, Algorithmic strategies for full waveform inversion: 1D experiments: Geophysics, **74**, no. 6, WCC37–WCC46.

Chan, T. F., G. H. Golub, and P. Mulet, 1999, A nonlinear primal-dual method for total variation-based image restoration: SIAM journal on scientific computing, **20**, 1964–1977.

Chen, Y., and S. Fomel, 2015, Random noise attenuation using local signal-and-noise orthogonalization: Geophysics, **80**, no. 6, WD1–WD9.

Daubechies, I., M. Defrise, and C. De Mol, 2004, An iterative thresholding algorithm for linear inverse problems with a sparsity constraint: Communications on Pure and Applied Mathematics, **57**, 1413–1457.

de Ribet, B., G. Yelin, Y. Serfaty, D. Chase, R. Kelvin, and Z. Koren, 2017, High resolution diffraction imaging for reliable interpretation of fracture systems: First Break, **35**, 43–47.

Decker, L., D. Merzlikin, and S. Fomel, 2017, Enhancing seismic-diffraction images using semblance-weighted least-squares migration: 87th Annual International Meeting, SEG, Expanded Abstracts, 5294–5299.

Dell, S., and D. Gajewski, 2011, Common-reflection-surface-based workflow for diffraction imaging: Geophysics, **76**, no. 5, S187–S195.

Dell, S., D. Gajewski, and A. Hoelker, 2019a, Azimuthal Diffraction Imaging: a Land Data Example from Northern Switzerland: Presented at the 81st EAGE Conference and Exhibition 2019.

Dell, S., A. Hoelker, and D. Gajewski, 2019b, Using seismic diffractions for assessment of tectonic overprint and fault interpretation: Geophysics, **84**, no. 1, IM1–IM9.

Fehmers, G. C., and C. F. Höcker, 2003, Fast structural interpretation with structure-oriented filtering: Geophysics, **68**, 1286–1293.

Fomel, S., 2002, Applications of plane-wave destruction filters: Geophysics, **67**, 1946–1960.

———, 2007, Shaping regularization in geophysical-estimation problems: Geophysics, **72**, no. 2, R29–R36.

Fomel, S., E. Landa, and M. T. Taner, 2007, Poststack velocity analysis by separation and imaging of seismic diffractions: Geophysics, **72**, no. 6, U89–U94.

Foss, S.-K., J. Matias, A. Sollid, L. Loures, T. Pinotti, E. Brenne, Ø. Wergeland, T. Broch, D. Merten, and N. Ettrich, 2018, Examples of geology from seismic diffractions: 88th Annual International Meeting, SEG, Expanded Abstracts, 4141–4145.

Glöckner, M., J. Walda, S. Dell, D. Gajewski, J. Karstens, D. Kläschen, and C. Berndt, 2019, Imaging zero-offset 3-D P-cable data with CRS method: Geophysical Journal International, **219**, 1876–1884.

Greer, S., and S. Fomel, 2018, Matching and merging high-resolution and legacy seismic images: Geophysics, **83**, no. 2, V115–V122.

Hale, D., 2009, Structure-oriented smoothing and semblance: CWP Report 635.

Harlan, W. S., J. F. Claerbout, and F. Rocca, 1984, Signal/noise separation and velocity estimation: Geophysics, **49**, 1869–1880.

Hoeber, H., K. Klem-Musatov, T. Moser, and M. Pelissier, 2010, Diffractions–A Historical Perspective: Expanded Abstracts 72nd EAGE International Conference, G033.

Kanasewich, E. R., and S. M. Phadke, 1988, Imaging discontinuities on seismic sections: Geophysics, **53**, 334–345.

Keller, J. B., 1962, Geometrical theory of diffraction: Journal of the Optical Society of America, **52**, 116–130.

Keydar, S., and E. Landa, 2019, Wave refocusing for linear diffractor using the time-reversal principle: Geophysical Prospecting, **67**, 1345–1353.

Klem-Musatov, K., 1994, Theory of Seismic Diffractions: Society of Exploration Geophysicists (Edited by Hron F. Fronta and Larry Lines).

Klem-Musatov, K. D., A. M. Aizenberg, J. Pajchel, and H. B. Helle, 2008, Edge and Tip diffractions: Theory and Applications in Seismic Prospecting: SEG Geophysical Monograph Series, **14**.

Klokov, A., R. Baina, and E. Landa, 2011, Point and edge diffractions in three dimensions: Expanded Abstracts 73rd EAGE International Conference, B023.

Klokov, A., and S. Fomel, 2012, Separation and imaging of seismic diffractions using migrated dip-angle gathers: Geophysics, **77**, no. 6, S131–S143.

———, 2013, Selecting an optimal aperture in Kirchhoff migration using dip-angle images: Geophysics, **78**, no. 6, S243–S254.

Klokov, A., A. Repnik, V. Bochkarev, and A. Bochkarev, 2017a, Integrated evaluation of Roseneath-Epsilon-Murteree formations, Cooper Basin, Australia to develop an optimal approach for sweet spot determination: Unconventional Resources Technology Conference (URTEC), Article ID 2670605.

Klokov, A., R. H. Treviño, and T. A. Meckel, 2017b, Diffraction imaging for seal evaluation using ultra high resolution 3D seismic data: Marine and Petroleum Geology, **82**, 85–96.

Koltanovsky, L., A. Korolev, E. Rossiyskaya, and K. Smirnov, 2017, Enhancing confidence in fracture prediction through advanced seismic data processing and analysis techniques: First Break, **35**, 49–53.

Koren, Z., and I. Ravve, 2011, Full-azimuth subsurface angle domain wavefield decomposition and imaging Part I: Directional and reflection image gathers: Geophysics, **76**, no. 1, S1–S13.

Kozlov, E., N. Barasky, E. Korolev, A. Antonenko, and E. Koshchuk, 2004, Imaging scattering objects masked by specular reflections: 74th Annual International Meeting, SEG, Expanded Abstracts, 1131–1134.

Landa, E., and S. Keydar, 1998, Seismic monitoring of diffraction images for detection of local heterogeneities: Geophysics, **63**, 1093–1100.

Liu, Y., S. Fomel, and G. Liu, 2010, Nonlinear structure-enhancing filtering using plane-wave prediction: Geophysical Prospecting, **58**, 415–427.

Meckel, T. A., and F. J. Mulcahy, 2016, Use of novel high-resolution 3D marine seismic technology to evaluate Quaternary fluvial valley development and geologic controls on shallow gas distribution, inner shelf, Gulf of Mexico: Interpretation, **4**, no. 1, SC35–SC49.

Merzlikin, D., and S. Fomel, 2015, An efficient workflow for path-integral imaging of seismic diffractions: 85th Annual International Meeting, SEG, Expanded Abstracts, 4096–4100.

———, 2016, Least-squares path-integral diffraction imaging using sparsity constraints: 86th Annual International Meeting, SEG, Expanded Abstracts, 4299–4304.

———, 2017, Analytical path-summation imaging of seismic diffractions: Geophysics, **82**, no. 1, S51–S59.

Merzlikin, D., S. Fomel, and A. Bona, 2016, Diffraction imaging using azimuthal plane-wave destruction: 86th Annual International Meeting, SEG, Expanded Abstracts, 4288–4293.

Merzlikin, D., S. Fomel, and M. K. Sen, 2019, Least-squares path-summation diffraction imaging using sparsity constraints: Geophysics, **84**, no. 3, S187–S200.

Merzlikin, D., S. Fomel, and X. Wu, 2018, Least-squares diffraction imaging using shaping regularization by anisotropic smoothing: 88th Annual International Meeting, SEG, Expanded Abstracts, 4326–4331.

Merzlikin, D., S. Fomel, X. Wu, and M. Phillips, 2017a, Unconventional reservoir characterization using azimuthal seismic diffraction imaging: Unconventional Resources Technology Conference (URTEC), Article ID 2695232.

Merzlikin, D., T. A. Meckel, S. Fomel, and Y. Sripanich, 2017b, Diffraction imaging of high-resolution 3D P-cable data from the Gulf of Mexico using azimuthal plane-wave destruction: First Break, **35**, 35–41.

Montazeri, M., L. O. Boldreel, A. Uldall, and L. Nielsen, 2020, Improved seismic interpretation of a salt diapir by utilization of diffractions, exemplified by 2D reflection seismics, Danish sector of the North Sea: Interpretation, **8**, no. 1, T77–T88.

Moser, T., 2011, Edge and tip diffraction imaging in three dimensions: Expanded Abstracts 73rd EAGE International Conference incorporating EUROPEC, B020.

Moser, T., L. Moskvil, E. Angerer, W. Kobusinski, M. Pelissier, and J. Orosz, 2020, Diffraction imaging of the Wisting Discovery: Fourth Naturally Fractured Reservoir Workshop, EAGE, 1–5.

Moser, T. J., and C. B. Howard, 2008, Diffraction imaging in depth: Geophysical Prospecting, **56**, 627–641.

Nemeth, T., C. Wu, and G. T. Schuster, 1999, Least-squares migration of incomplete reflection data: Geophysics, **64**, 208–221.

Papziner, U., and K.-P. Nick, 1998, Automatic detection of hyperbolas in georadargrams by slant-stack processing and migration: First Break, **16**, 219–223.

Pelissier, M., T. J. Moser, C. Yu, J. Lang, I. Sturzu, and A. M. Popovici, 2017, Interpretation value of diffractions and sub-specular reflections–applications on the Zhao Dong field: First Break, **35**, 61–68.

Popovici, A. M., I. Sturzu, and T. J. Moser, 2015, High resolution diffraction imaging of small scale fractures in shale and carbonate reservoirs: 14th International Congress of the Brazilian Geophysical Society, SPE–178538–MS.

Rad, P. B., B. Schwarz, C. Vanelle, and D. Gajewski, 2014, Common reflection surface (CRS) based pre-stack diffraction separation: 84th Annual International Meeting, SEG, Expanded Abstracts, 4208–4212.

Reshef, M., and E. Landa, 2009, Post-stack velocity analysis in the dip-angle domain using diffractions: Geophysical Prospecting, **57**, 811–821.

Ronen, S., and C. L. Liner, 2000, Least-squares DMO and migration: Geophysics,

65, 1364–1371.

Schoepp, A., S. Labonté, and E. Landa, 2015, Multifocusing 3D diffraction imaging for detection of fractured zones in mudstone reservoirs: case history: Interpretation, **3**, no. 1, SF31–SF42.

Schwarz, B., 2019, Coherent wavefield subtraction for diffraction separation: Geophysics, **84**, no. 3, V157–V168.

Schwarz, B., and D. Gajewski, 2017, Accessing the diffracted wavefield by coherent subtraction: Geophysical Journal International, **211**, 45–49.

Serfaty, Y., L. Itan, D. Chase, and Z. Koren, 2017, Wavefield separation via principle component analysis and deep learning in the local angle domain: 87th Annual International Meeting, SEG, Expanded Abstracts, 991–995.

Silvestrov, I., R. Baina, and E. Landa, 2015, Poststack diffraction imaging using reverse-time migration: Geophysical Prospecting, **64**, 129–142.

Strong, D., and T. Chan, 2003, Edge-preserving and scale-dependent properties of total variation regularization: Inverse Problems, **19**, S165–S187.

Sturzu, I., A. M. Popovici, T. J. Moser, and S. Sudhakar, 2015, Diffraction imaging in fractured carbonates and unconventional shales: Interpretation, **3**, no. 1, SF69–SF79.

Taner, M. T., S. Fomel, and E. Landa, 2006, Separation and imaging of seismic diffractions using plane-wave decomposition: 76th Annual International Meeting, SEG, Expanded Abstracts, **25**, 2401–2405.

Tsingas, C., B. E. Marhfoul, S. Satti, and A. Dajani, 2011, Diffraction imaging as an interpretation tool: First Break, **29**, no. 12, 57–61.

Tyiasning, S., D. Merzlikin, D. Cooke, and S. Fomel, 2016, A comparison of diffraction imaging to incoherence and curvature: The Leading Edge, **35**, 86–89.

Van Vliet, L. J., and P. W. Verbeek, 1995, Estimators for orientation and anisotropy in digitized images, *in* Proceedings of the First Annual Conference of the Advanced School for Computing and Imaging ASCI'95: 442–450.

Weickert, J., 1997, A review of nonlinear diffusion filtering: International Conference on Scale-Space Theories in Computer Vision, Springer, 1–28.

——, 1998, Anisotropic diffusion in image processing: Teubner.

Wu, X., 2017, Directional structure-tensor-based coherence to detect seismic faults and channels: Geophysics, **82**, no. 2, A13–A17.

Wu, X., and X. Janson, 2017, Directional structure tensors in estimating seismic structural and stratigraphic orientations: Geophysical Journal International, **210**, 534–548.

Yu, C., J. Zhao, and Y. Wang, 2017a, Seismic detection method for small-scale discontinuities based on dictionary learning and sparse representation: Journal of Applied Geophysics, **137**, 55–62.

Yu, C., J. Zhao, Y. Wang, and Z. Qiu, 2016, Sparse diffraction imaging method using an adaptive reweighting homotopy algorithm: Journal of Geophysics and Engineering, **14**, 26–40.

Yu, C., J. Zhao, Y. Wang, C. Wang, and W. Geng, 2017b, Separation and imaging diffractions by a sparsity-promoting model and subspace trust-region algorithm: Geophysical Journal International, **208**, 1756–1763.

Zelewski, G., W. A. Burnett, E. Liu, M. Johns, X. Wu, J. Zhang, and G. Skeith, 2017, Diffraction imaging enhancement using spectral decomposition for faults, fracture zones, and collapse feature detection in a Middle East carbonate field: First Break, **35**, 55–60.

Znak, P., S. Dell, B. Kashtan, and D. Gajewski, 2019, Identification and focusing of edge diffractions with wavefront attributes: 89th Annual International Meeting, SEG, Expanded Abstracts, 5060–5064.